Alteration and paragenesis of the basalt-hosted Au deposits, southwestern Guizhou Province, China: Implications for ore genesis and exploration

Junhai Li [a,b,c], Pan Wu [a], Zhuojun Xie [d,*], Jianzhong Liu [c,e], Shuangju Zhang [f], Weifang Song [a], Bingqiang Zhang [b], Songtao Li [g], Liangyi Xu [b], Lulin Zheng [h]

[a] College of Resources and Environmental Engineering, Guizhou University, Guiyang 550025, China
[b] No.105 Geological Party, Guizhou Bureau of Geology and Mineral Exploration & Development, Guiyang 550018, China
[c] Innovation Center of Ore Resources Exploration Technology in the Region of Bedrock, Ministry of Natural Resources of People's Republic of China, Guiyang 550081, China
[d] State Key Laboratory of Ore Deposit Geochemistry, Institute of Geochemistry, Chinese Academy of Sciences, Guiyang 550081, China
[e] Guizhou Bureau of Geology and Mineral Exploration & Development, Guiyang 550004, China
[f] Guizhou Institute of Technology, Guiyang 550003, China
[g] School of Geography and Resources, Guizhou Education University, Guiyang 550018, China
[h] Mining College, Guizhou University, Guiyang 550025, China

ARTICLE INFO

ABSTRACT

Carlin-type Au deposits are dominantly hosted in sedimentary rocks. Recent exploration has identified two deposits (Jiadi and Damaidi) hosted in the Emeishan basalt in southwestern Guizhou Province, China, that contain Carlin-type mineralization. In this study, ore and alteration minerals from the two deposits were examined, mineral parageneses were established through detailed petrography, whole-rock chemistry and mineralogical studies, and results were compared with the sediment-hosted Carlin-type Au deposits.

In both deposits, pre-ore stage minerals are mainly igneous minerals in basalt, including orthopyroxene, clinopyroxene, plagioclase, magnetite, and minor ilmenite and apatite. These minerals formed during the eruption and formation of the Emeishan Large Igneous Province. The Au ore-stage mineral assemblage consists of arsenian pyrite, arsenopyrite, illite, jasperoid quartz, (Fe)-dolomite (locally Ca-Mg-siderite), rutile, and apatite. This transition indicates that pre-ore basalt was altered to minerals that characterize Carlin-type ore.

Electron probe microanalysis and laser ablation-inductively coupled plasma-mass spectrometry analyses show that the arsenian pyrite and arsenopyrite contain ~457 ppm and ~556 ppm Au, respectively, and are enriched in As, Cu, Sb, Hg, and Tl. Gold is ionically bound in the disseminated arsenian pyrite and arsenopyrite which formed during sulfidation. During the late-ore stage, open space-filling realgar, calcite, quartz, stibnite, and orpiment precipitated as the hydrothermal system cooled and collapsed. Post-ore stage minerals include hematite and chlorite, reflecting post-ore oxidation.

Comparison studies indicate the two deposits share remarkable similarities to the Guizhou sediment-hosted Carlin-type Au deposits. The basalt-hosted and sediment-hosted Au deposits in Dian-Qian-Gui area formed in response to the same widespread metallogenic event. This study confirms that basalt can host Carlin-type Au mineralization. Future exploration for Carlin-type Au deposits in Dian-Qian-Gui area can be expanded into regions dominated by basalt, especially the anticlines above the unconformity between the Maokou limestone and Emeishan basalt.

1. Introduction

Carlin-type Au deposits, mainly located in Nevada, USA, and Dian-Qian-Gui area, China (Fig. 1; Muntean and Cline, 2018), account for ~8% of annual worldwide Au production (Frimmel, 2008). One of the most significant characteristics of Carlin-type Au deposits is that they are dominantly hosted in the silty calcareous sedimentary rocks because these rocks commonly contain large mass of carbonaceous silty
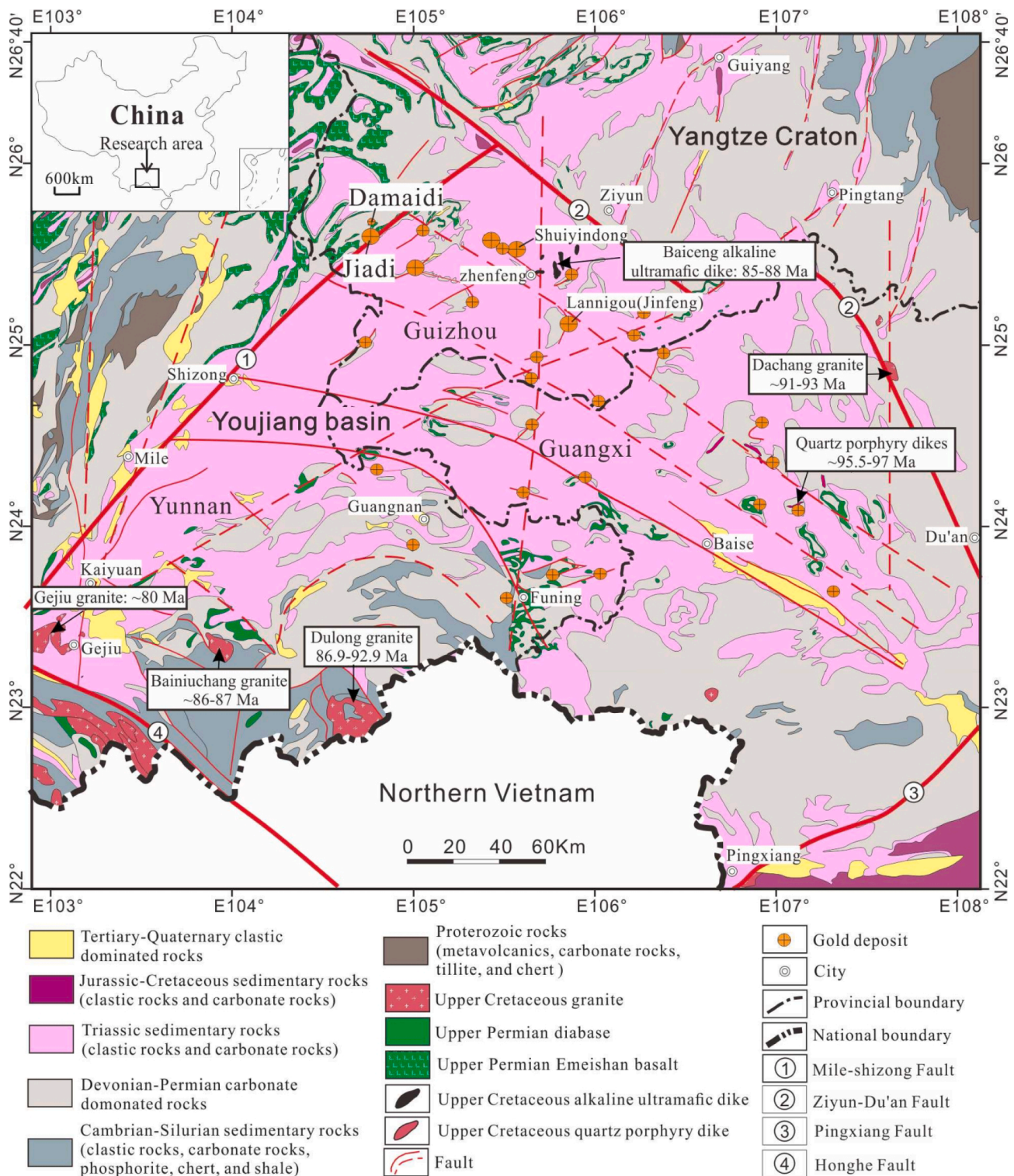
Fig. 1. Regional geologic map showing the distribution of Carlin-type Au deposits in the Dian-Qian-Gui area, China (modified from Su et al., 2018).

carbonate and good permeability, making them easily reacting with the acidic or near-neutral ore fluids (Hofstra and Cline, 2000; Cline et al., 2005; Su et al., 2018). Additionally, the calcareous sedimentary rocks are generally enriched in Fe, providing essential Fe for sulfidation and formation of Au-bearing pyrite and arsenopyrite (Hofstra et al., 1991; Stenger et al., 1998; Kesler et al., 2003; Ye et al., 2003; Su et al., 2009; Xie et al., 2018a).

Recent exploration discovered two primary Au deposits, including Jiadi and Damaidi, hosted in the Emeishan basalt in southwestern

Guizhou Province (Fig. 1), although a few small oxidized Au deposits were discovered and mined in this district since 1990's. The two deposits are described as exhibiting some characteristics typical of Carlin-type Au mineralization. Wang (2015) conducted a geochemical study on the Jiadi deposit, and results show that (1) the ore assemblage consists of pyrite, arsenopyrite, quartz, and clay minerals; (2) anomaly elements in ore include Au, As, Hg, Tl, and Sb; and (3) the deposit formed from low-temperature (~210℃) and low-salinity (~6 wt% NaCl) ore fluid. Zeng et al. (2018) studied the structures and ore fluid pathways of the Jiadi
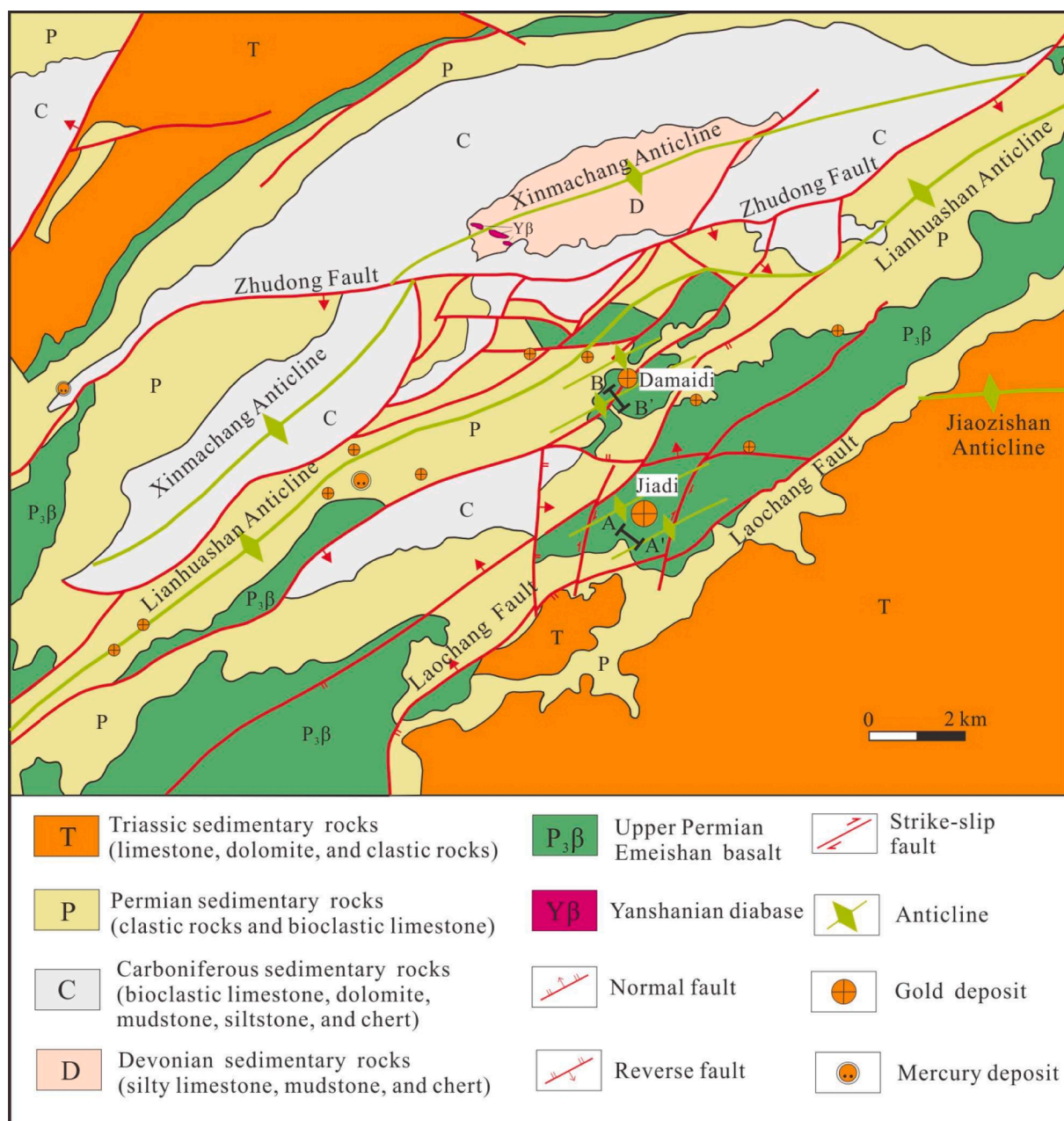
Fig. 2. Geological map of the Lianhuashan anticline illustrating the location of the Jiadi and Damaidi deposits. Lines A-A' and B-B' mark the location of the cross sections shown in Figs. 3 and 4, respectively.

deposit by integrating field geological investigations and structural analysis. Results indicate that deep ore fluids migrated vertically to shallow crust along regional faults, and subsequently flowed horizontally into the interformational fracture zones and outward into the steep micro fractures, and precipitated Au. Additionally, Hu et al. (2018) quantified the chemistry and S isotope compositions of pyrite and arsenopyrite from the Jiadi and Damaidi deposits, and results show that ore-stage pyrite and arsenopyrite have elevated Au, As, Sb, and Cu, and a narrow range of $\delta^{34}S$ values (pyrite: $-2.8 \sim 2.1‰$; arsenopyrite: $0.4 \sim 7‰$). Results also show that the ore-stage pyrite and arsenopyrite have trace elements associations similar to the framboidal pyrite, which led them to suggest that the Emeishan basalt provided not only ore-forming space but also ore-forming elements for Au mineralization (Hu et al., 2018). In summary, previous studies on the basalt-hosted Au deposits mainly focused on geological and geochemical descriptions, structure analyses, sulfides chemistry, and S isotope compositions analyses.

However, the alteration minerals and alteration processes associated with Au mineralization are yet to be identified, and the mineral paragenesis remains yet to be established. The alteration process is key to understanding the genesis of the deposit, and significant for exploration of this type deposit in the basalt area.

In this study, we conducted detailed petrography, geochemical, and mineralogical studies on the Jiadi and Damaidi deposits. We identified the alteration minerals and alteration processes, established the mineral parageneses, and compared the two deposits with the sediment-hosted Carlin-type Au deposits in Dian-Qian-Gui area (from here on referred to as Guizhou sediment-hosted Carlin-type Au deposits). This study suggests the basalt-hosted and sediment-hosted Au deposits in Dian-Qian-Gui area formed in response to the same widespread metallogenic event. Additionally, this study demonstrates that basalt is a potential host rock for Carlin-type Au mineralization. Future exploration for Carlin-type Au deposits in Dian-Qian-Gui area should be expanded to
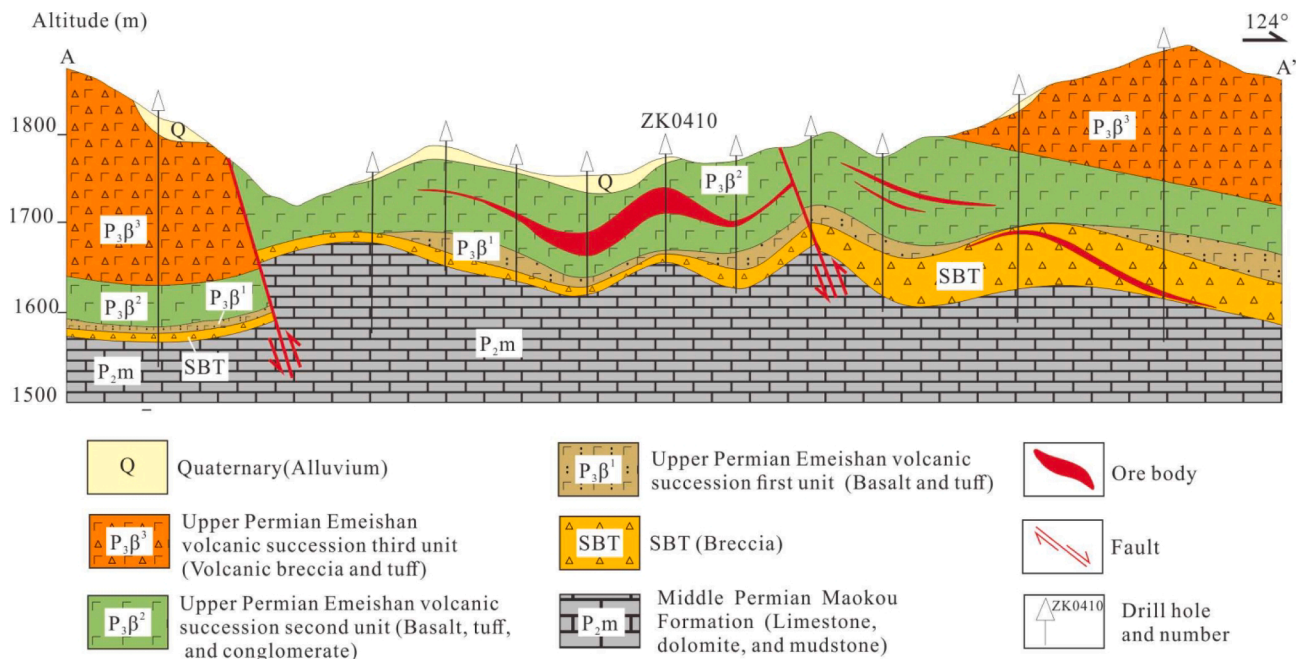
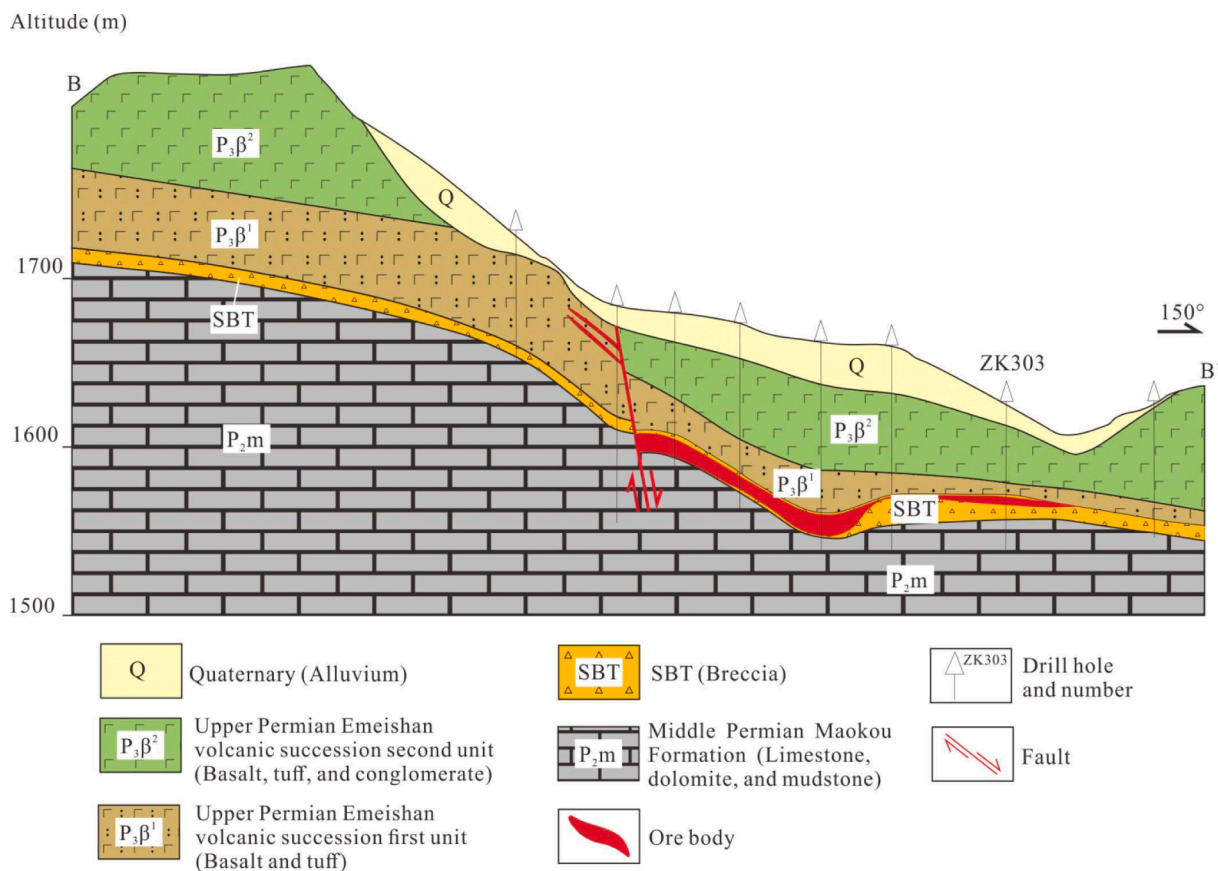Fig. 3. Geological cross section of No. 4 exploration line in the Jiadi deposit.

Fig. 4. Geological cross section of No. 3 exploration line in the Damaidi deposit.
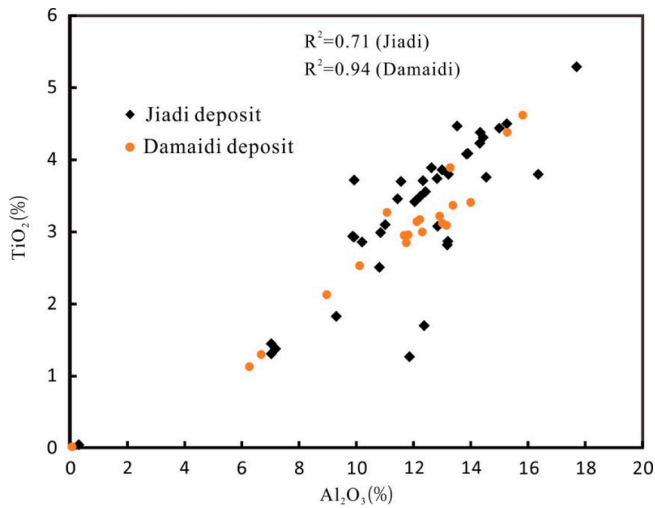
Fig. 5. Plot of the concentrations of TiO_2 vs. Al_2O_3 from the Jiadi and Damaidi deposits. Original data are included in Table A1. The high positive correlations ($R^2 = 0.71$ for Jiadi and 0.94 for Damaidi) indicate these species are immobile components at both deposits.

include regions covered by basalt.

2. Geological background

2.1. Characteristics of Guizhou Carlin-type Au deposits

Almost all Guizhou Carlin-type Au deposits are located within the Youjiang Basin (Fig. 1). These deposits share remarkably similar characteristics including the following which are mainly summarized from Su et al. (2018) and Xie et al. (2018a; 2018b). (1) The deposits exhibit structural and stratigraphic controls. Almost all deposits are hosted within carbonate-bearing rocks, and controlled by faults, unconformities, and/or anticlines (Chen et al., 2011; Su et al., 2018; Wang and Groves, 2018; Xie et al., 2018a; Yang et al., 2020). (2) Most Au was originally structurally bound in the trace element-rich arsenian pyrite and arsenopyrite (Chen et al., 2009; Su et al., 2012; Xie et al., 2018a; Yan et al., 2018; Liang et al., 2020; Wei et al., 2020). (3) Alteration associated with Au mineralization includes dissolution of calcite, jasperoid quartz replacement of calcite, minor illite replacement of K-bearing minerals, and sulfidation of Fe in Fe-dolomite to form Au-bearing pyrite, arsenopyrite, and dolomite (Su et al., 2018; Xie et al., 2018a). In particular, ore-stage minerals are disseminated in ore instead of
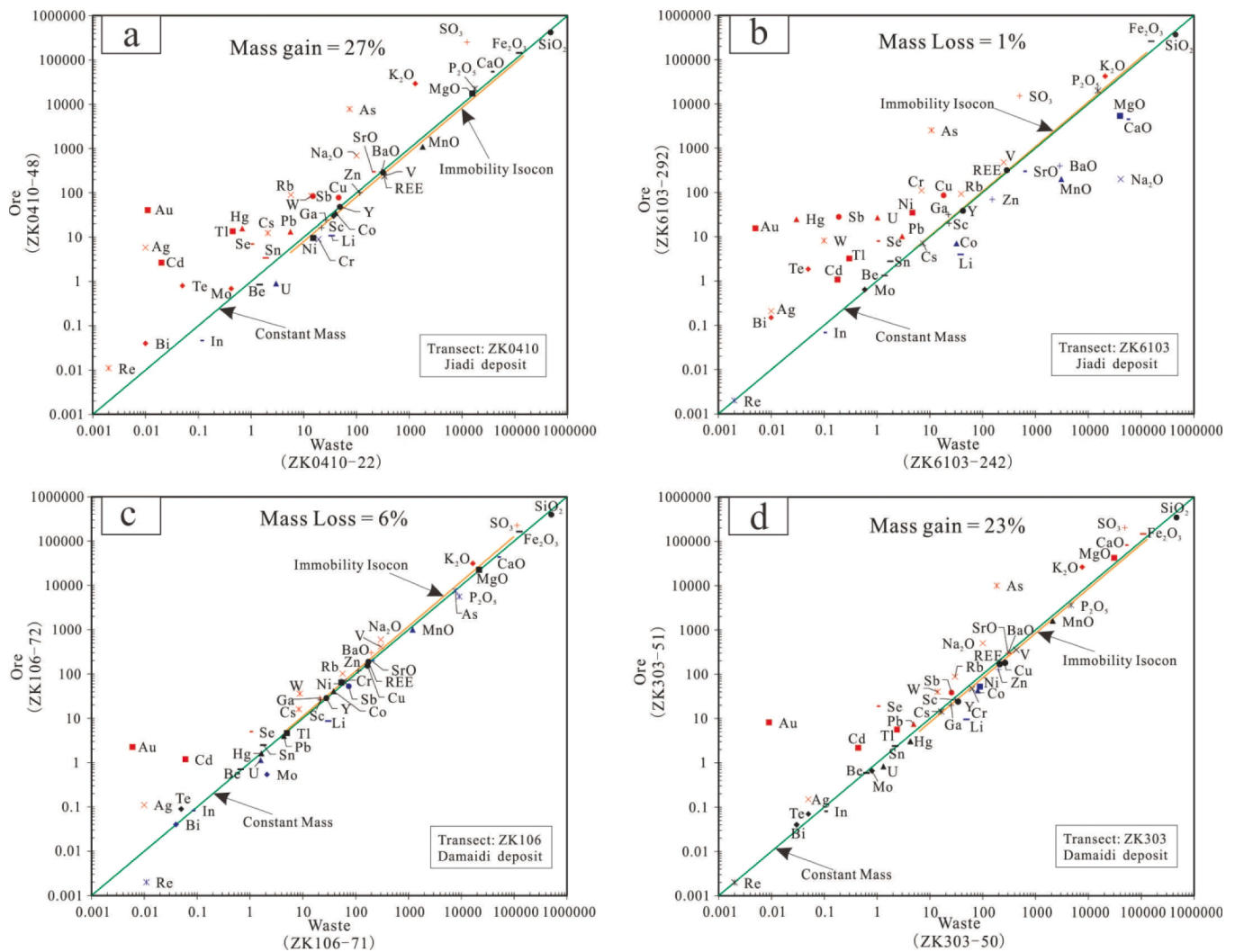
Fig. 6. Isocon diagrams showing elemental fluxes and mass transfer associated with Au mineralization at the Jiadi (a, b) and Damaidi (c, d) deposits. All values are in ppm, and included in Table A1. The immobility isocon is the line of best fit through the concentrations of TiO_2, Al_2O_3, Zr, Hf, and Nb. The net mass change is calculated by the equation: $\triangle$mass (%) = [(1/m)-1]*100, where m is the slope of the immobility isocon from the transect (Hofstra, 1994). The position of the isocon relative to the line of constant mass is a measure of change in mass of host rock. Transects ZK0410 (a) and ZK6103 (b) exhibit significant Au, As, Hg, Tl, Sb, Cu, SO_3, and K_2O are added at the Jiadi deposit. Transects ZK106 (c) and ZK303 (d) show Au, Cd, Ag, SO_3, and K_2O are consistently added, and Tl, Hg, As, MgO, and CaO are either added or remain nearly constant at the Damaidi deposit.

Fig. 7. Variation of major and Carlin-suite elements (Au, As, Sb, Hg, Tl, and Cu) along the selected part of drill hole ZK0410 from the Jiadi deposit. The location of drill hole is shown in Fig. 3. All data are included in Table A1. The Carlin-suite elements, K_2O, SO_3, and CaO have coordinated variation.

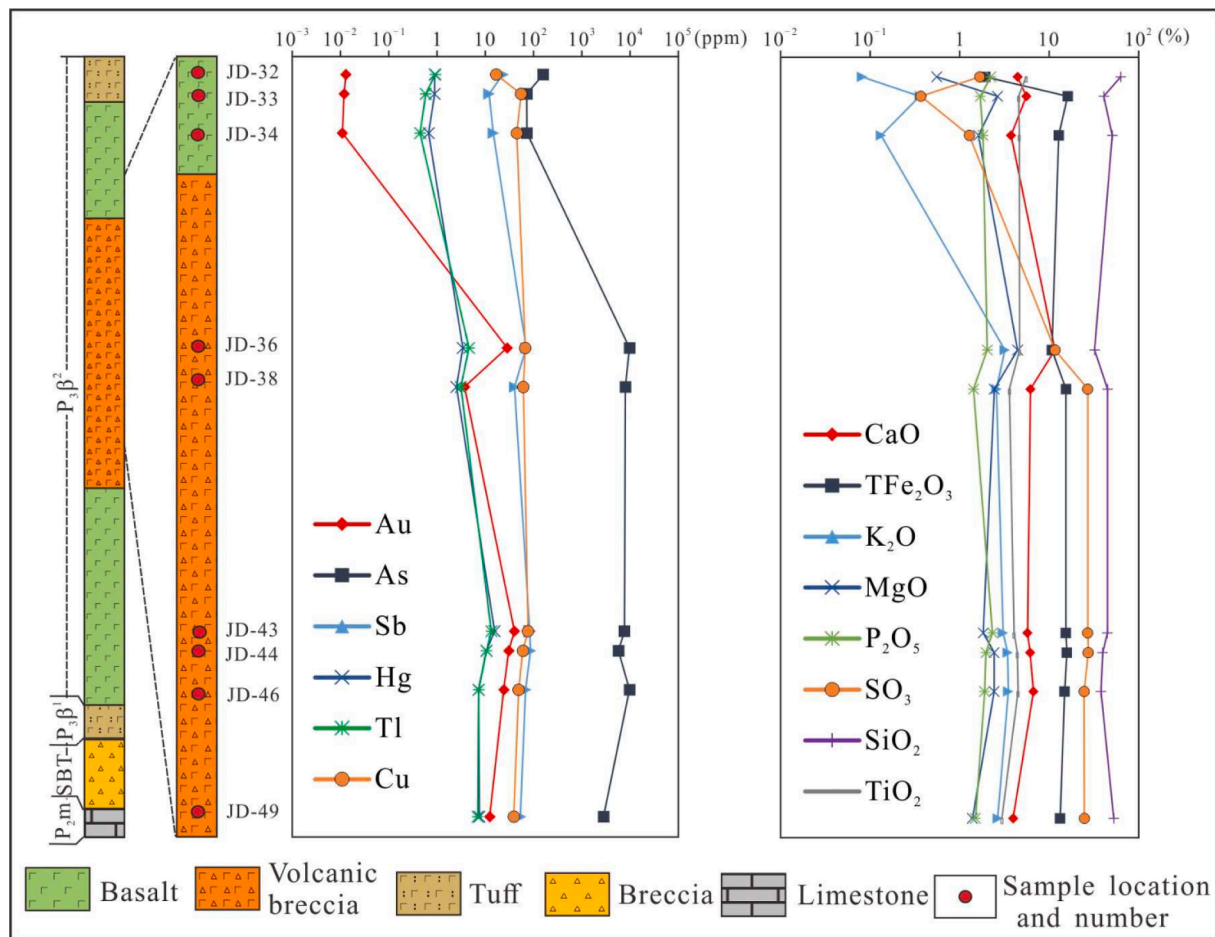occurring as veins. (4) Late-ore stage realgar, calcite, quartz, stibnite, and orpiment precipitated in open space as the hydrothermal system cooled and collapsed (Tan et al., 2015b; Su et al., 2018; Xie et al., 2018a). (5) Signature ore elements that characterize these deposits include Au, As, Sb, Hg, Tl, and Cu, with low to absent Ag and base metals. No known coeval porphyry, skarn, or distal Ag-Pb-Zn mineralization has been identified proximal to the deposits (Hu et al., 2002; Su et al., 2018; Xie et al., 2018a). (6) The deposits commonly formed at depths of 2–8 km and at temperatures of 190–300 °C (average ~ 250 °C) from low-salinity (<~5 wt% NaCl equiv.), CO_2-rich (6–75 mol %), reduced, and non-boiling ore fluids (Zhang et al., 2003; Su et al., 2009, 2018). (7) Compared with the typical Carlin-type Au deposits in Nevada, USA, Guizhou Carlin-type Au deposits contain more abundant ore-stage dolomite and arsenopyrite (Xie et al., 2018a, 2018b). Dolomite-stable alteration formed from less acidic, CO_2-rich ore fluids at higher temperature and pressure, compared to the Nevada Carlin-type deposits, and reflects conditions intermediate to typical Nevada Carlin-type deposits and orogenic systems (Cline et al., 2013; Xie et al., 2018a, 2018b). Guizhou Carlin-type deposits may represent a link between orogenic and classic Carlin-type gold deposits (Cline et al., 2013; Su et al., 2018; Xie et al., 2018a, 2018b).

2.2. Regional geology

The Youjiang basin is roughly defined by the Mile-Shizong, Ziyun-Du'an, Pingxiang, and Honghe faults (Fig. 1). The tectonic setting of the Youjiang basin is summarized from Su et al. (2018) and Xie et al.

(2018a). The basin was produced by Early Devonian passive margin rifting of the southwest margin of the Precambrian Yangtze craton. The rifting event produced a series of NE- and NW-striking high-angle basement-penetrating normal faults that controlled subsequent sedimentation, deformation, and magmatism. From the Devonian to Triassic, a passive margin sequence developed on the continental margin. In the northwestern part of the basin, platform-facies sedimentary rocks dominated by carbonate rocks and terrigenous detrital rocks were deposited. In the eastern and southern part of the basin, a sequence of deeper-water slope/basin-facies calcareous sedimentary rocks formed. Following passive margin deposition, W-verging subduction of the Pacific plate beneath the Eurasian plate began during the mid-Permian (Li and Li, 2007) and NE-verging subduction of the Meso-Tethys ocean beneath Sibumasu began during the Early Cretaceous (Lai et al., 2014; Zaw et al., 2014) folded the basin sequence, and these two tectonic events may related to the formation of the Au deposits (Su et al., 2018; Xie et al., 2018a).

Several igneous rocks including Emeishan basalt, diabases, granites, quartz porphyry dikes, and alkaline ultramafic dikes are exposed in the Youjiang basin (Fig. 1). The Upper Permian Emeishan basalt is exposed in the northwest margin of the basin. It belongs to the Emeishan Large Igneous Province, and erupted at ~260 Ma (Zhou et al., 2002, 2006; Guo et al., 2004; Zhong and Zhu, 2006). The Emeishan volcanic succession covers an area of $>5*10^5$ km^2, and southeastward terminated at the northwest margin of the Youjiang basin (Zhou et al., 2002). The rift-related Upper Permian diabase is mainly exposed in the south part of the basin. Several Upper Cretaceous granites (~80–95.6 Ma), quartz

porphyry dikes (95–97 Ma), and alkaline ultramafic dikes (85–88 Ma) intruded the sedimentary rocks and are related to the basin extension (Su et al., 2018; Xie et al., 2018a and references therein). Most of these granites and dikes are ~20 to >100 km from the Au deposits (Fig. 1). Only at the Liaotun Au deposit in the southeastern part of the Youjiang Basin is there an unaltered quartz porphyry dike that crosscuts the Au orebody (Chen et al., 2014).

To date, the accurate mineralization age for the Guizhou Carlin-type Au deposits remains controversial. Hu et al. (2017) review the Au mineralization age, and suggested that these deposits formed mostly at 200–230 Ma (Indosinian orogeny) and were overprinted by the Yanshanian orogeny (130–160 Ma). Su et al. (2018) and Xie et al. (2018a) discuss ages proposed for Au mineralization using different methods and conclude that the most reliable proposed ages are based on crosscutting relationships. Thus, they suggested that Au mineralization that formed the Carlin-type Au deposits in the Youjiang basin occurred between Jurassic and Late Cretaceous time.

2.3. Geology of the Jiadi Au deposit

The Jiadi deposit, located ~36 km southeast of the town of Panzhou City, Guizhou Province, China, has proven and probable Au resources of >60 tonnes (t) with an average grade of 2–3 g/t (105 Geological Party, Guizhou Bureau of Geology and Mineral Exploration & Development, unpublished report, 2018). The deposit is currently in the detailed exploration stage, and has yet to be mined. Geologically, the Jiadi deposit lies along the northwestern margin of the Youjiang basin (Fig. 1).

The Jiadi deposit is controlled by the tectonic zones with multiple folds of the southeast limb of Lianhuashan anticline (Fig. 2). The ENE trending Lianhuashan anticline is ~10–20 km wide and ~45 km long with both limbs dipping at low angles (Fig. 2; Liu, 2002). The northwest limb of the anticline is monoclinal, however, the southeast limb is strongly deformed and folded. Several Au deposits are controlled by these crumpled tectonic zones with multiple folds of the southeast limb (Fig. 2).

The stratigraphy at the Jiadi deposit is composed of the Middle Permian Maokou and Upper Permian Longtan sedimentary rocks and Upper Permian Emeishan basalt (Figs. 2, 3). Gold mineralization mainly occurs in the Emeishan basalt and the unconformity (SBT) between the Emeishan basalt/Longtan Formation and the underlying Maokou Formation (Fig. 3). The Moukou Formation with a thickness of ~290 m mainly consists of thick-layer limestone interbedded with dolomite and locally carbonaceous mudstone. The Longtan Formation, lying above the Moukou Formation, mainly occurs in the south of the deposit. It is dominated by grey mudstone and siltstone, with basalt gravel and tuff at the base. Locally, coal seams occur in this formation.

The Emeishan basalt unconformably overlies the Moukou Formation (Fig. 3). The Emeishan volcanic succession in Jiadi district has a thickness of 150–350 m, and was divided into three units according to the lithologic characteristics (Fig. 3). The lower (first) unit is dominated by dark green massive basalt interbedded with dark grey tuff. The middle (second) unit consists of grey massive basalt, basaltic tuff, and basaltic conglomerate. The upper (third) unit is mainly composed of volcanic breccia, with sedimentary tuff at the base. Igneous rocks except the Emeishan basalt have yet to be identified by geologic mapping or drilling in the Jiadi deposit. A few diabase dikes ~7 km from the deposit intruded into the sedimentary rocks (Fig. 2).

Gold mineralization of Jiadi is mainly strata-bound, and two layers of strata-bound orebodies were recognized (Fig. 3). The upper orebody preferentially occurs in the basaltic conglomerate and basaltic tuff of the middle unit of Emeishan basalt. The rocks above and below the orebody are typically massive basalt. The lower orebody is controlled by the regional SBT (Fig. 3). The SBT also hosts some low-grade strata-bound orebodies in a number of Au deposits in southwestern Guizhou province (Liu et al., 2010, 2014). Additionally, the SBT was proposed as the

regional structural conduit that fed ore fluids for the formation of upper Au mineralization (Liu et al., 2010, 2014; Tan et al., 2015a).

2.4. Geology of the Damaidi Au deposit

The Damaidi deposit has proven and probable Au resources of 6 t with an average grade of 3–4 g/t, and has yet to been mined (105 Geological Party, Guizhou Bureau of Geology and Mineral Exploration & Development, unpublished report, 2013). The Damaidi deposit is located at ~4 km north from the Jiadi deposit (Fig. 2), and exhibits geological characteristics remarkably similar to the Jiadi deposit.

Stratigraphy at the Damaidi deposit includes the middle Permian Maokou and upper Permian Longtan sedimentary rocks and upper Permian Emeishan basalt (Fig. 2). The lithologic characteristics of these formations in the Damaidi deposit are similar to that in the Jiadi deposit. The Damaidi deposit is controlled by the tectonic zones with multiple folds of the southeast limb of Lianhuashan anticline, similar to the Jiadi deposit (Fig. 2).

The main difference between the Damaidi and Jiadi deposits is that Au mineralization of Damaidi mainly occurs in the SBT between the Emeishan basalt and Maokou Formation, and the first unit of Emeishan basalt (Fig. 4), however, Au mineralization of Jiadi preferentially occurs in the second unit of Emeishan basalt and the SBT (Fig. 3).

3. Methods

3.1. Sample collection

Approximately 151 samples were collected from drill core and outcrop from the Jiadi and Damaidi deposits. Gold assays were examined from drill logs to identify sample transects that transition from low or below detection Au into high-grade rock. Short sample transects minimize variations in primary lithology such that alteration and texture can be more confidently related to hydrothermal events. Most samples in this study were collected from drill core along short transects.

3.2. Major and trace element analyses

Pulps of 58 samples were analyzed for major and trace elements at the ALS Chemex (Guzangzhou) Co. Ltd (Table A1). Major elements were analyzed using a PANalytical PW2424 X-ray fluorescence spectrometer. Loss on ignition (LOI) was obtained using 1 g powder and heating to 1100 °C for 1 h. Trace elements were detected using an Agilent 7700x inductively coupled plasma-mass spectrometry (ICP-MS). For low- and medium-grade samples (Au: 0.005–10 ppm), Au was assayed using a Varian Spectr AA240 atomic absorption spectroscopy. For high-grade samples (Au: >10 ppm), Au was first tested by fire assay method, and then analyzed using the gravimetric method. Mercury analysis was performed using an Agilent 7900 ICP-MS. The analytical precision for all elements was better than 5%. Detection limits for the analyzed elements are listed in Table A1.

3.3. Optical petrography

A total of 50 polished thin sections were prepared for petrography observation. All sections were scanned using a Leica DM4P microscope equipped with an electric scanning platform at the State Key Laboratory of Ore Deposit Geochemistry, Institute of Geochemistry, Chinese Academy of Sciences (IGCAS). The textural relationship and overall characteristic of ore and host rock are readily apparent on the section scan. Transmitted and reflected-light microscopy was then used to identify mineralogy and alteration and determine the mineral paragenesis.

3.4. Scanning electron microscopy

A FEI Scios dual beam scanning electron microscope (SEM) at the

Center for Lunar and Planetary Sciences, IGCAS, was used to confirm and identify minerals, and observe mineral textures. Backscattered electrons (BSE) images were captured to illustrate textures and provide precise locations for electron probe microanalysis (EPMA) and laser ablation-inductively coupled plasma-mass spectrometry (LA-ICP-MS) analysis.

3.5. Electron probe microanalysis

Eight polished sections were probed using a JEOL JXA-8230 EPMA at the State Key Laboratory of Ore Deposit Geochemistry, IGCAS. Analyzed elements in pyrite and arsenopyrite include Fe, Cu, Zn, Co, Ni, Bi, Au, As, S, Sb, Hg, Tl, Te, and Pb. Operating conditions include a 25 kV accelerating voltage, 2–5 μm spot size, and 10 nA beam current. Standards and detection limits for these analyses are presented in Table A2.

3.6. Laser ablation-inductively coupled plasma-mass spectrometry

Pyrite and arsenopyrite from three polished sections were analyzed using a LA-ICP-MS at the Nanjing FocuMS Technology Co. Ltd. A Teledyne Cetac Technologies Analyte Excite laser-ablation system was coupled to an Agilent Technologies 7700x quadrupole ICP-MS. The 193 nm ArF excimer laser, homogenized by a set of beam delivery systems, was focused on sulfide surface with fluence of 3.5 J/cm^2. The ablated

material was transported to ICP-MS by He carrier gas. USGS polymetal sulfide pressed pellet MASS-1 and synthetic basaltic glasses GSE-1G were combined for external calibration. In this study, single ablation was performed using a 20 or 25 μm at 6 Hz repetition rate for 30 s. Detection limits for these analyses are provided in Table A2.

4. Results and interpretations

4.1. Mass transfer associated with Au mineralization

Elemental fluxes and mass transfer associated with mineralization and alteration can be recognized by a comparison of host rock to the mineralized counterpart using isocon diagrams (Gresens, 1967; Grant, 1986). A key step for creating the immobility isocon diagram is to determine the immobile elements and further determine the immobility isocon. Element immobility and mobility can be identified using X-Y concentration plots, and the immobile elements commonly form a straight line that passes through the origin (Finlow-Bates and Stumpfl, 1981). The plot of concentrations of TiO$_2$ vs. Al$_2$O$_3$ produces a linear regression with high R^2 value (0.94 for Daimaidi and 0.71 for Jiadi) that passes through the origin (Fig. 5), which suggests the immobile behavior of both elements at both deposits. In addition, Zr, Hf, and Nb exhibit similar immobile behaviors, and are commonly chosen as immobile elements in fluid-rock interaction (Cail and Cline, 2001; Guo et al., 2012;
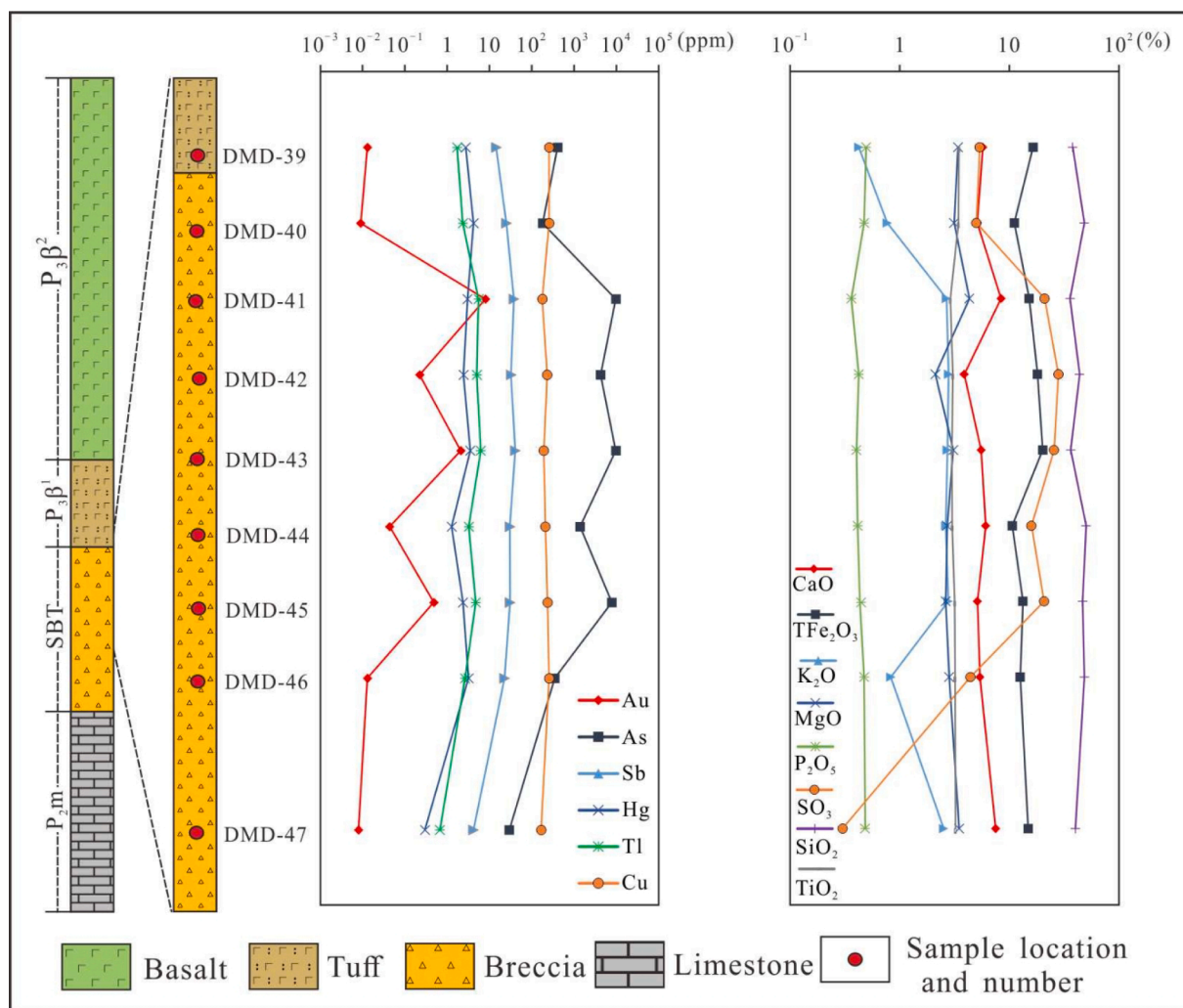

Fig. 8. Variation of major and Carlin-suite elements (Au, As, Sb, Hg, Tl, and Cu) along the selected part of drill hole ZK303 from the Damaidi deposit. The location of drill hole is indicated in Fig. 4. All data are listed in Table A1. Arsenic, Sb, Hg, Tl, Cu, K$_2$O, and SO$_3$ increase as Au grade increases.

Table 1
Spearman rank correlation matrix of partial major and trace elements of whole rock analysis from the Jiadi and Damaidi deposits.

	Au	As	Sb	Hg	Tl	Cu	SO_3	Al_2O_3	CaO	TFe_2O_3	K_2O	MgO	MnO	Na_2O	P_2O_5	SiO_2	SrO	TiO_2	Ag	Cd	Rb	Se	Te
As	**0.70**																						
Sb	**0.45**	**0.77**																					
Hg	**0.63**	**0.81**	**0.83**																				
Tl	**0.60**	**0.89**	**0.83**	**0.89**																			
Cu	0.06	0.18	0.22	0.17	0.32																		
SO_3	**0.52**	**0.81**	**0.56**	**0.69**	**0.77**	0.30																	
Al_2O_3	0.08	0.24	0.20	0.30	**0.41**	0.38	0.30																
CaO	-0.22	-0.25	**-0.43**	**-0.45**	**-0.43**	-0.09	-0.28	-0.37															
TFe_2O_3	0.14	0.29	0.03	0.22	0.39	**0.41**	**0.42**	**0.83**	-0.29														
K_2O	**0.51**	**0.54**	0.31	**0.47**	**0.63**	0.31	**0.49**	**0.49**	-0.26	**0.57**													
MgO	-0.04	-0.12	**-0.51**	-0.27	-0.19	0.13	0.10	0.26	**0.80**	**0.40**	0.20												
MnO	-0.21	-0.06	-0.37	-0.29	-0.20	0.04	0.00	0.24	**0.69**	0.32	0.02	0.39											
Na_2O	-0.05	-0.22	**-0.53**	**-0.51**	0.15	-0.26	-0.11	0.23	0.14	0.34	0.23	**0.46**	-0.10										
P_2O_5	0.04	0.07	0.03	0.14	0.15	0.15	0.00	**0.59**	-0.16	**0.45**	0.26	0.12	0.24	0.12									
SiO_2	0.15	0.29	0.32	0.33	**0.45**	0.30	0.31	**0.81**	0.31	**0.63**	**0.40**	-0.04	-0.10	0.14	0.37								
SrO	0.02	-0.19	**-0.58**	**-0.40**	-0.32	-0.07	-0.13	-0.05	**-0.59**	0.20	-0.03	**0.61**	**0.56**	**0.57**	-0.03	-0.13							
TiO_2	0.10	0.25	0.14	0.30	**0.40**	0.28	0.34	**0.98**	0.39	**0.84**	**0.50**	0.34	0.29	0.26	**0.65**	**0.78**	0.01						
Ag	**0.78**	**0.55**	**0.57**	**0.62**	**0.63**	0.36	0.39	0.13	-0.35	0.11	**0.44**	-0.24	-0.29	-0.11	-0.01	0.17	-0.15	0.09					
Cd	**0.50**	0.37	**0.49**	**0.42**	**0.49**	**0.40**	0.24	-0.06	-0.26	-0.09	0.32	-0.33	-0.37	-0.13	-0.27	0.01	-0.31	-0.15	**0.71**				
Rb	**0.52**	**0.60**	0.35	**0.51**	**0.67**	0.34	**0.54**	**0.52**	-0.23	**0.61**	**0.99**	0.23	0.08	0.18	0.26	**0.42**	-0.03	**0.53**	**0.45**	0.31			
Se	**0.67**	**0.72**	**0.72**	**0.61**	**0.71**	0.29	**0.47**	0.17	**-0.50**	0.14	0.39	**-0.45**	**-0.43**	-0.12	-0.10	0.33	-0.26	0.11	**0.70**	**0.61**	**0.40**		
Te	**0.70**	0.35	**0.43**	**0.42**	0.35	0.06	0.02	0.07	-0.18	-0.04	0.34	-0.32	-0.32	-0.13	0.17	0.17	-0.19	0.01	**0.74**	**0.52**	0.32	**0.56**	
W	**0.65**	**0.83**	**0.79**	**0.89**	**0.87**	0.19	**0.71**	0.39	-0.37	0.31	**0.43**	-0.12	-0.12	**-0.43**	0.20	**0.41**	-0.33	**0.41**	**0.59**	**0.51**	**0.51**	**0.61**	0.38

Values > 0.4 and < -0.4 are in bold. N = 58 (38 analyses from Jiadi and 20 analyses from Damaidi; Complete data are included in Table A3. Data used to calculate the Spearman rank correlation matrix are listed in Table A1.

Tan et al., 2015a). Thus, in this study we choose Al, Ti, Zr, Hf, and Nb as immobile elements during creating immobility isocon diagrams, and the immobility isocon is the line of best fit through the concentrations of TiO_2, Al_2O_3, Zr, Hf, and Nb. Elements that plotting along the immobility isocon suggest no net change in concentration or immobility. Elements that lie above the immobility isocon are added to the rock during Au mineralization and alteration. Elements that plotting below the immobility isocon are removed from the rock.

In this study, element concentrations of the highest Au grade sample from a transect were plotted against the lowest Au grade sample in the immobility isocon diagrams. The two samples were collected from the same formation (Emeishan basalt or SBT) and exhibit similar lithologic characteristics (Fig. 6; Table A1). Four isocon diagrams were created and evaluated for four sample transects, with two from Jiadi and two from Damaidi (Fig. 6). At the Jiadi deposit (Fig. 6a; 6b), Au, As, Hg, Tl, Sb, Cu, SO_3, and K_2O have been significantly and consistently added to the original rock. Minor Bi, Te, Se, Cd, and Ag are variably added. SiO_2, Fe_2O_3, and P_2O_5 remain nearly constant. MgO and CaO are either removed from the rock or remain nearly constant. At the Damaidi deposit (Fig. 6c; 6d), Au, Cd, Ag, K_2O, and SO_3 are consistently added to the original rock. MgO, CaO, Tl, Hg, and As are either added or remain nearly constant. Similar to the Jiadi, SiO_2, Fe_2O_3, and P_2O_5 from the Damaidi are almost unchanged.

The net mass change is calculated by the equation: $\triangle$mass (%) = [(1/m)-1]*100, where m is the slope of the immobility isocon from the transect (Hofstra, 1994). At both Jiadi and Damaidi, the mass change of the host rock varies between transects, and the variation is not significant (<50%; Fig. 6). The mass change shows no correlation to change in Au concentration.

Figs. 7 and 8 document the variation of major and Carlin-suite elements (Au, As, Sb, Hg, Tl, and Cu) along a drill hole from the Jiadi and Damaidi deposits, respectively. At the Jiadi deposit (Fig. 7), the Carlin-suite elements have nearly consistent variation. Additionally, K_2O, SO_3, and CaO increase as Au grade increases. However, SiO_2, Fe_2O_3, MgO, TiO_2, and P_2O_5 remain nearly constant. At the Damaidi deposit (Fig. 8), Au and As contents have obvious coordinated variation. Antimony, Hg, Tl, and Cu increase slightly, and SO_3 and K_2O increase significantly as Au grade increases. SiO_2, Fe_2O_3, CaO, MgO, TiO_2, and P_2O_5 are almost constant as Au grade varies.

A Spearman rank correlation matrix was constructed by using major and trace element data of whole-rock analyses from both deposits (Tables 1 and A3). Gold correlates positively (>0.4) with As (0.70), Sb (0.45), Hg (0.63), Tl (0.60), SO_3 (0.52), K_2O (0.51), Ag (0.78), Cd (0.50), Rb (0.52), Se (0.67), Te (0.70), and W (0.65) (Table 1). In addition, the correlation coefficients between two Carlin-suite elements except Cu are >0.4 (Table 1). Most correlation coefficients between Carlin-suite elements and SO_3, K_2O, Ag, Cd, Rb, Se, Te, and W are >0.4 (Table 1). Strong negative correlations (<-0.4) between Carlin-suite elements and other elements include CaO and Sb (-0.43), CaO and Hg (-0.45), CaO and Tl (-0.43), MgO and Sb (-0.51), Na_2O and Sb (-0.53), Na_2O and Hg (-0.51), SrO and Sb (-0.58), and SrO and Hg (-0.40) (Table 1).

Plotting of Fe vs. S contents of whole-rock analyses (Fig. 9) shows that the low-grade samples (Au: <0.1 ppm) have variable Fe and S, and S in most low-grade samples is <2%. Most medium- (Au: 0.1–1 ppm) and high-grade (Au: >1 ppm) samples contain high concentrations of Fe and S (Fig. 9). Moreover, most data plot along the sulfidation trend instead of along the pyritization line.

Integrated isocon diagrams (Fig. 6), drill hole profile figures (Figs. 7; 8), and Spearman rank correlation matrix table (Table 1) show that the Carlin-suite element except Cu, including Au, As, Sb, Hg, and Tl, were significantly and consistently added, and trace Bi, Te, Se, Cd, and Ag were variably added at the Jiadi and Damaidi deposits. K_2O was significantly added at both deposits and possibly related to the formation of illite during argillization, a typical alteration process of Carlin-type mineralization (Hofstra and Cline, 2000; Cail and Cline, 2001; Su et al., 2018; Xie et al., 2018a). The nearly constant CaO indicates that
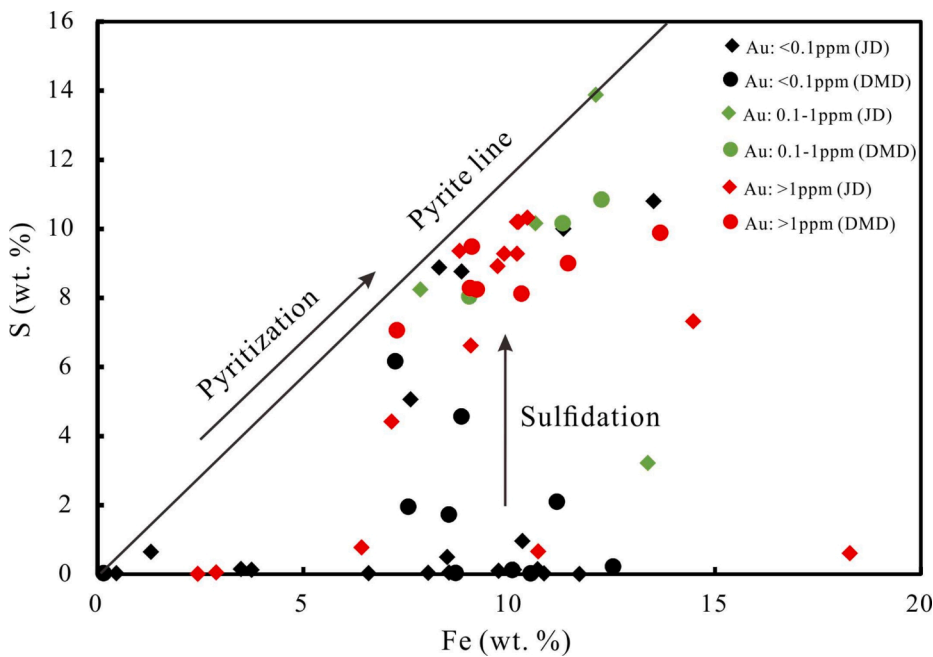
Fig. 9. Plot of Fe vs. S contents from the Jiadi and Damaidi deposits. All data are included in Table A1. The pyritization line indicates the addition of both S and Fe, and the sulfidation line indicates the addition of S. Low-grade samples (Au: <0.1 ppm) have variable Fe and S, and the S in most low-grade samples is <2%. Most medium- (Au: 0.1–1 ppm) and high-grade (Au: >1 ppm) samples contain high concentrations of Fe and S, and the data plot along the sulfidation trend. Abbreviations: JD = Jiadi deposit, DMD = Damaidi deposit.

decalcification, a key alteration process of Carlin-type mineralization (Hofstra and Cline, 2000; Cline et al., 2005; Maroun et al., 2017; Su et al., 2018; Xie et al., 2018a), is insignificant at both deposits, which is consistent with the insignificant variation of mass change. Iron vs. S plots (Fig. 9) and the variation of Fe and S during Au mineralization (Figs. 6; 7; 8) demonstrate that sulfidation instead of pyritization accounts for the formation of ore-stage pyrite and arsenopyrite.

4.2. Paragenesis, mineral textures and chemistry

Sample transects from low- to high-grade rocks were examined to identify the mineral paragenesis. Integrated whole-rock analyses, petrography, and SEM, EPMA and LA-ICP-MS analyses show that three events occur at the Jiadi and Damaidi deposits, including pre-ore formation of Emeishan basalt, subsequent Au hydrothermal mineralization and alteration, and locally post-ore oxidation (Fig. 10).

4.2.1. Pre-ore stage minerals

Pre-ore stage minerals mainly consist of minerals in the basalt. The unmineralized basalt at both deposits exhibits assemblage of basalt and contains abundant orthopyroxene, clinopyroxene, plagioclase, and magnetite, and minor ilmenite and apatite (Fig. 11). These minerals make up the main pre-ore stage minerals at both deposits (Fig. 10). Whole-rock analyses show the basalt contains high concentrations of Fe_2O_3 (~14 wt%), Al_2O_3(~14 wt%), CaO (~7 wt%), TiO_2 (~3 wt%), and MgO (~3 wt%) (Table A1). Additionally, SEM EDS detected high concentrations of Fe (~20 wt%), Mg (~9 wt%), and Al (~8 wt%) in orthopyroxene, high concentrations of Ca (~19 wt%), Mg (~9 wt%), Fe (~9 wt%), Al (~2 wt%), and Ti (~1 wt%) in clinopyroxene, and minor Fe (~1 wt%) and Mg (~1 wt%) in plagioclase. Calcite is locally observed in brecciated basaltic tuff samples collected from the SBT. This calcite is from the underlying Maokou limestone.

4.2.2. Ore-stage minerals, ore pyrite and arsenopyrite chemistry, and alteration

The ore stage is defined as the major period of deposition of Au-bearing pyrite and arsenopyrite (Xie et al., 2018a). The ore-stage minerals and alteration at the Jiadi and Damaidi deposits are similar (Fig. 10).

Gold-bearing arsenian pyrite is disseminated in medium- and high-grade ore (Fig. 12a; 12b). Arsenian pyrite, commonly 10–100 μm in diameter, has a yellowish color, bright reflectivity, and good polish (Fig. 13a; 13b). Chemical zoning is rarely observed using reflected-light petrography and BSE imaging (Fig. 13a; 13b). Locally, oscillatory zoning is apparent under BSE imaging adjusted for low brightness and high contrast (Fig. 13e), and the brighter part corresponds to the higher As concentration. The euhedral-subhedral arsenian pyrite is commonly intergrown with arsenopyrite, illite, quartz, (Fe)-dolomite, apatite, and rutile (Figs. 13d; 12e; 12f; 13f).

Electron probe microanalysis and LA-ICP-MS analysis indicate the arsenian pyrite contains variable Au ranging from 0.01 to 3160 ppm, with a mean value of 457 ppm calculated from EPMA data (Fig. 13b; 13 g; Table 2). Additionally, EPMA data indicate that the arsenian pyrite contains ~1.6 wt% As, ~158 ppm Cu, and ~78 ppm Sb (Table 3). Mercury and Tl are commonly below the EPMA detection (Hg: ~800 ppm; Tl: ~550 ppm) (Table 3). However, LA-ICP-MS analyses indicate that Hg and Tl in the arsenian pyrite range from several to 101 ppm, and several to 38 ppm, respectively (Fig. 13b; Table 2).

Arsenopyrite, also an important Au-bearing mineral at both deposits, is commonly disseminated in medium- and high-grade ore (Figs. 12b; 13c; 13d). The subhedral to euhedral arsenopyrite has a diameter of 5–100 μm, yellowish-white color, bright reflectivity, and good polish (Fig. 13c). Arsenopyrite generally has an unhomogeneous brightness under the BSE imaging adjusted for low brightness and high contrast (Fig. 13d; 13e). The core is darker than the rim because of lower concentration of As in the core, and the boundary between the core and rim is irregular (Fig. 13c; 13d; 13e; 13h; Table 4). Locally, arsenopyrite rims arsenian pyrite (Figs. 12f; 3f).

Gold in arsenopyrite ranges from below EPMA detection (~500 ppm) to 2800 ppm, with an average of 556 ppm (Tables 3 and A4). Electron probe microanalysis data indicate that As in arsenopyrite varies from 33.3 to 45.4 wt%, with an average value of 40.4 wt% (Tables 3 and A4). Arsenopyrite is enriched in Cu (avg = 212 ppm), Sb (avg = 227 ppm), and Tl (avg = 82 ppm) (Table 3). Mercury in arsenopyrite is below the EPMA detection (~800 ppm) (Table 3), however, LA-ICP-MS detected tens of ppm Hg.

Illite is absent from low-grade basalt, but abundant in medium- and high-grade ore (Fig. 12c-f). Illite occurs as a lamellar aggregate

Mineral	Jiadi and Damaidi			
	Pre-ore stage	Ore forming event		Post-ore stage
		Ore stage	Late-ore stage	
Orthopyroxene	▬▬			
Clinopyroxene	▬▬			
Plagioclase	▬▬			
Magnetite	▬▬			
Ilmenite	▬▬			
Apatite	▬▬			
Arsenian pyrite		▬▬		
Arsenopyrite		▬▬		
Jasperoid quartz		▬▬		
Illite		▬▬		
(Fe)-dolomite		▬▬		
Ca-Mg-siderite		·······		
Rutile		▬▬		
Apatite		▬▬		
Vein calcite			▬▬	
Realgar			▬▬	
Stibnite			▬▬	
Vein quartz			▬▬	
Orpiment			▬▬	
Chlorite				▬▬
Hematite				▬▬

Fig. 10. Mineral paragenesis for the Jiadi and Damaidi Au deposits. The two deposits have the same mineral paragenesis.

(Figs. 12d; 13f), and commonly encompasses arsenopyrite and arsenian pyrite, or is surrounded by quartz (Figs. 12c-f; 13f).

Jasperoid quartz has an irregular boundary and good polish (Fig. 12c-d). It is abundant in ore (Fig. 12c-e) and absent from the low-grade basalt (Fig. 11). Jasperoid quartz generally encompasses arsenopyrite, arsenian pyrite, and illite. Fine-grained apatite and rutile disseminated in jasperoid quartz is generally observed.

(Fe)-dolomite is a common gangue mineral observed in ore (Fig. 12c-e), and absent from low-grade basalt. (Fe)-dolomite has an irregular boundary, and is intergrown with jasperoid quartz, arsenopyrite, and arsenian pyrite (Fig. 12c-e). Iron in (Fe)-dolomite, determined by SEM EDS analyses, ranges from below detection (~1 wt%) to 14 wt% (commonly 5–12 wt%). Locally, Fe in the dolomite-like mineral reaches up to 34 wt%, and Ca and Mg in the mineral are ~2–4 wt%, which suggests the mineral is more likely Ca-Mg-rich siderite instead of Fe-dolomite.

Rutile, absent from low-grade basalt, is commonly observed in ore (Fig. 12c-d). Rutile is less abundant than illite, quartz, and (Fe)-dolomite in ore. It has an irregular boundary and abundant pore space filled with

quartz, illite, or (Fe)-dolomite (Fig. 12c-d). Rutile is generally intergrown with quartz, (Fe)-dolomite, and illite.

Minor apatite is present in the Au ore, commonly as <20 μm subhedral to anhedral grains enclosed by jasperoid quartz, (Fe)-dolomite, and illite (Fig. 12c-e). Regardless of the fact that the basalt host rock contains minor apatite, the amount of apatite in ore increases as Au grade increases.

From low-grade basalt to medium- and high-grade ore, the mineral assemblage transitioned from plagioclase-orthopyroxene-clinopyroxene- magnetite-ilmenite-apatite to arsenian pyrite-arsenopyrite-illite-jasperoid quartz-(Fe)-dolomite (locally Ca-Mg-siderite)-rutile-apatite (Figs. 11; 12; 14). The transition resulted from Au mineralization and alteration, and demonstrates that arsenian pyrite, arsenopyrite, illite, jasperoid quartz, (Fe)-dolomite (locally Ca-Mg-siderite), rutile, and partial apatite precipitated during the ore stage (Fig. 10; 14). Results also indicate that arenian pyrite and arsenopyrite are the dominating Au-bearing minerals at both deposits, and they formed during sulfidation of Fe from the basalt, most possibly from the ilmenite, orthopyroxene, and clinopyroxene (Fig. 14). Dolomite-stable
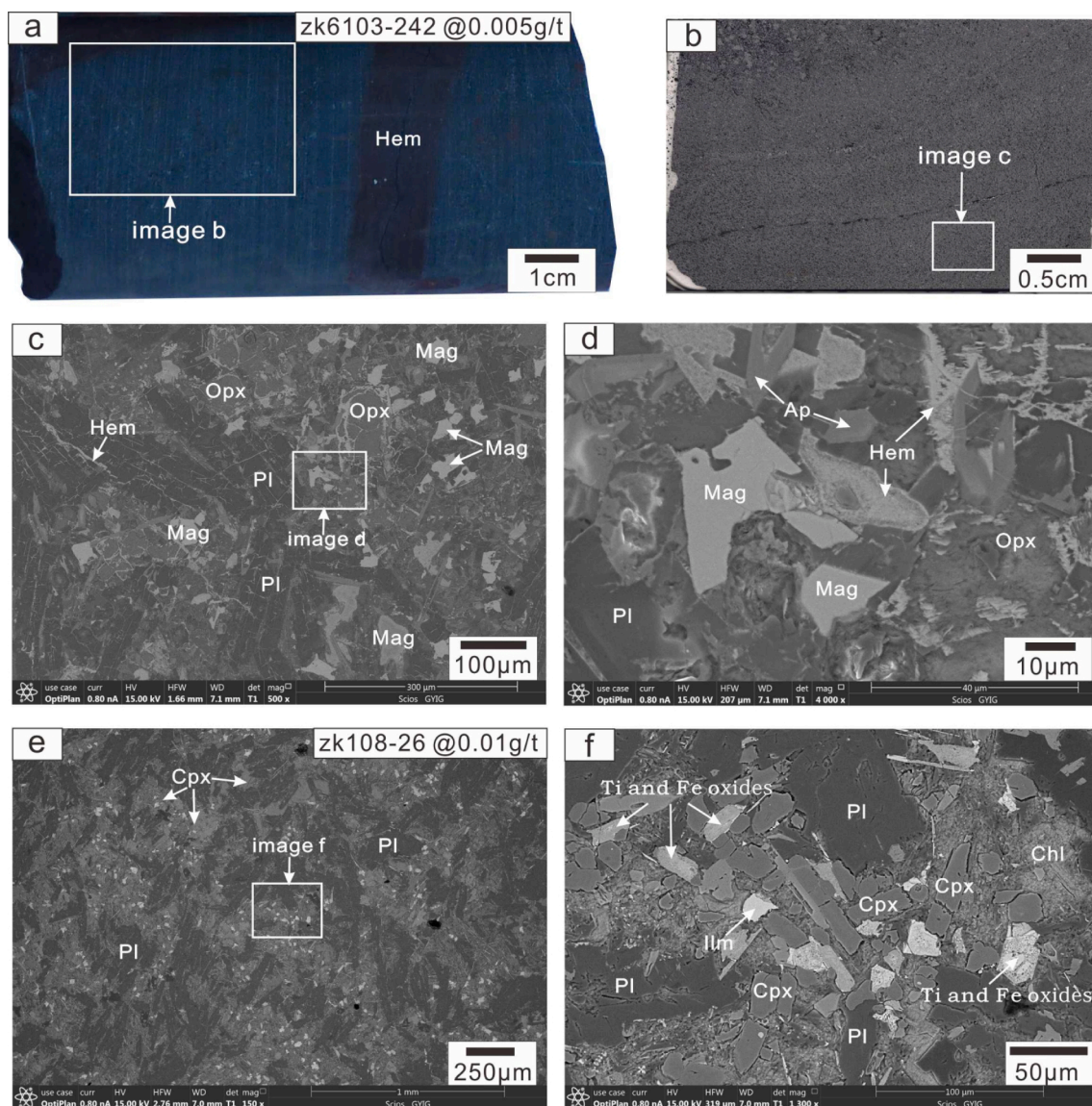
Fig. 11. Images of low-grade basalt from the Jiadi (a-d) and Damaidi (e, f) deposits. The label in the top right of images a and e indicates the sample number, consisting of the drill hole number and sampling depth (meter), and the Au grade. a-d. A low-grade basalt from the Jiadi deposit is composed primarily of plagioclase, orthopyroxene, and magnetite, and minor apatite. Hematite occurs along a veinlet and is disseminated in the basalt. The hematite is possibly oxidized from the magnetite, pyrite, and/or arsenopyrite. a: hand sample image; b: polished section scan image; c-d: backscattered electron images. e-f. Backscattered electron images show a low-grade basalt from the Damaidi deposit consisting of plagioclase, clinopyroxene, and ilmenite. Minor chlorite and Ti-Fe oxides (f), most likely oxidized plagioclase and ilmenite, respectively, are observed. Abbreviations: Ap = apatite, Chl = chlorite, Cpx = clinopyroxene, Hem = hematite, Ilm = ilmenite, Mag = magnetite, Opx = orthopyroxene, Pl = plagioclase.

alteration reflects a near-neutral ore fluid of Guizhou Carlin-type Au deposit (Xie et al., 2017, 2018a). The near-neutral ore fluid reacted with orthopyroxene, clinopyroxene, and plagioclase, leading to the formation of illite, jasperoid quartz, and (Fe)-dolomite (Fig. 14). Note that the source of potassium required for the formation of illite was the ore fluid because whole-rock analyses indicate potassium was significantly added to the ore (Figs. 6; 7; 8). Silicon for formation of jasperoid quartz was likely from the alteration of orthopyroxene, clinopyroxene, and plagioclase during ore-stage fluid-rock reaction because the Si content for both low- and high-grade rocks are nearly constant (Figs. 6; 7; 8).

4.2.3. Late-ore stage minerals

The late-ore stage minerals in Carlin-type Au deposits reflect hydrothermal cooling and collapse (Hofstra et al., 1991; Cline et al., 2005). Abundant realgar and calcite fill fractures in both ore and low-grade

rock at the Jiadi and Damaidi deposits (Fig. 15a). Stibnite and quartz commonly occur as veins adjacent to the orebody (Fig. 15b-c). Locally, orpiment is intergrown with realgar. Integrated the spatial relationship of these minerals with ore and the mineral chemical composition suggest that these minerals are related to Au mineralization, and precipitated during the late-ore stage (Fig. 10). Late-ore stage minerals occur in fractures or as veins indicating open-space precipitation (Hofstra et al., 1991; Cline, 2001; Xie et al., 2018a).

4.2.4. Post-ore stage oxidation

Post-ore stage minerals at the Jiadi and Damaidi deposits include some oxide minerals and chlorite (Fig. 10). These minerals are mainly observed in the samples collected from outcrop and shallow levels of some drill holes. Hematite occurs along small fractures, is disseminated in basalt (Fig. 11a; 11d), and could have replaced magnetite, pyrite,
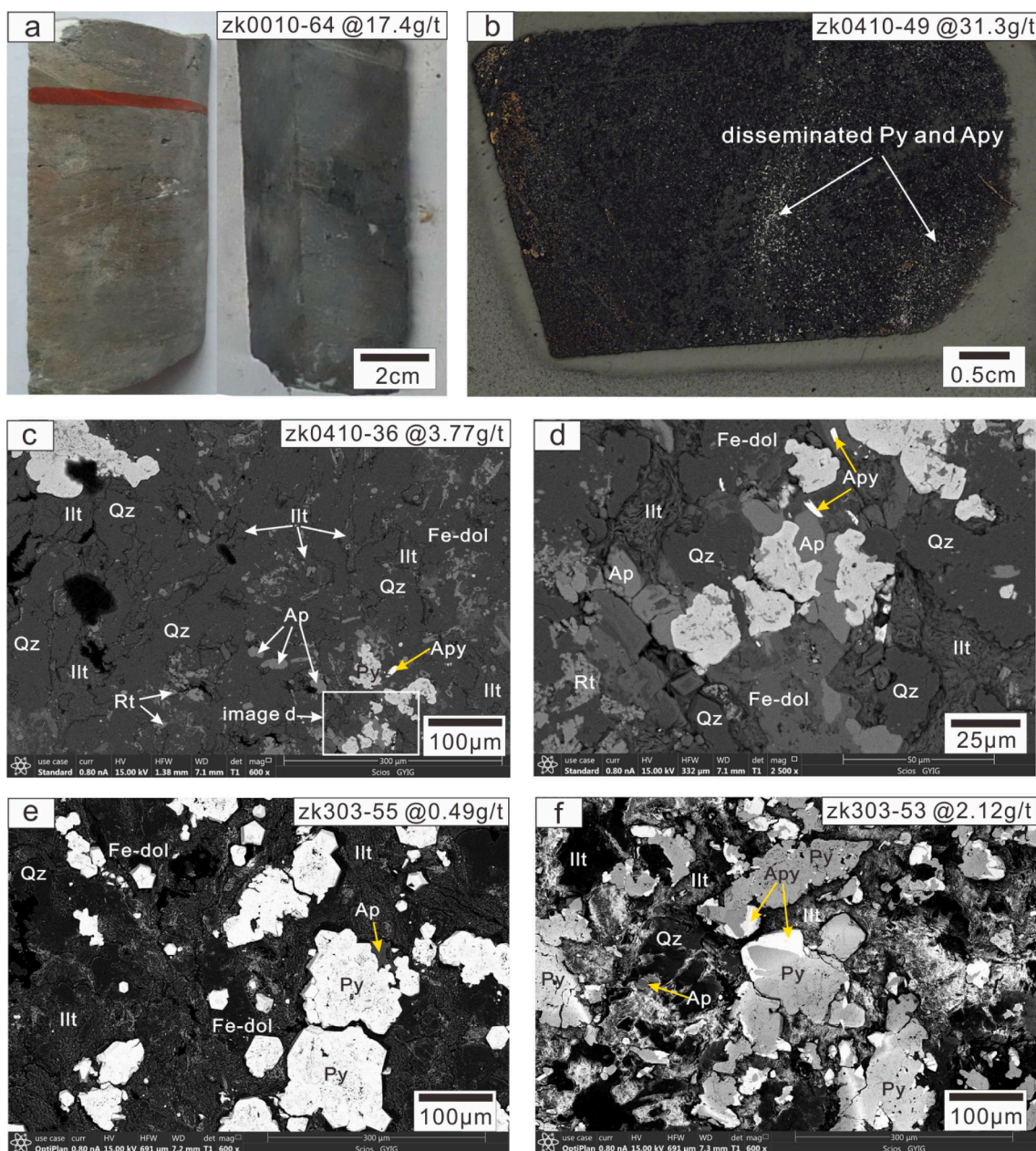
Fig. 12. Images of medium–high grade ore from the Jiadi (a-d) and Damaidi (e-f) deposits showing mineral assemblages and alteration associated with Au mineralization. The label in the top right of image indicates the sample number, consisting of drill hole number and sampling depth (meter), and Au grade. a. Hand sample image shows the characteristics of massive ore. Visible porosity and veins are absent. b. Polished section scan image shows abundant disseminated pyrite and arsenopyrite in high-grade ore. c-d. Medium grade ore from the Jiadi is composed of jasperoid quartz, illite, Fe-dolomite, pyrite, arsenopyrite, apatite, and rutile. Disseminated pyrite and arsenopyrite are commonly surrounded by quartz, illite, Fe-dolomite, apatite, and rutile (backscattered electron images). e. Low-medium grade ore from the Damaidi shows abundant illite and quartz encompassing pyrite (backscattered electron image). f. Medium grade ore from the Damaidi exhibits abundant illite, quartz, pyrite, and minor arsenopyrite. Locally, pyrite is rimmed by arsenopyrite (backscattered electron image). Abbreviations: Ap = apatite, Apy = arsenopyrite, Fe-dol = Fe-dolomite, Ilt = illite, Py = pyrite, Qz = quartz, Rt = rutile.

and/or arsenopyrite during supergene oxidation. Minor chlorite present in low-grade basalt (Fig. 11f) is possibly oxidized from plagioclase during post-ore stage. Minor minerals display textures similar to the ilmenite (Fig. 11f), however, SEM EDS analyses show the chemical composition is a mixture of hematite and rutile, which indicates that these minerals are the oxidation product of ilmenite.

5. Comparison of the Jiadi and Damaidi deposits with Guizhou sediment-hosted Carlin-type Au deposits

Table 5 summarizes the characteristics of the basalt-hosted (Jiadi and Damaidi) and Guizhou sediment-hosted Carlin-type Au deposits. The basalt-hosted Au deposits share many characteristics of Guizhou sediment-hosted Carlin-type Au deposits, mainly including the following. (1) The basalt-hosted Au deposits formed in a tectonic setting similar to the sediment-hosted Carlin-type Au deposits because both are located in the Youjiang basin or on the margin of the basin. This region
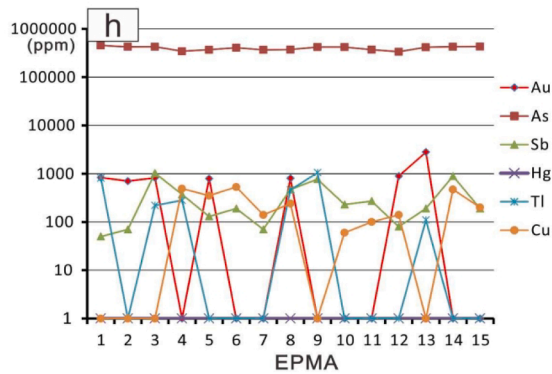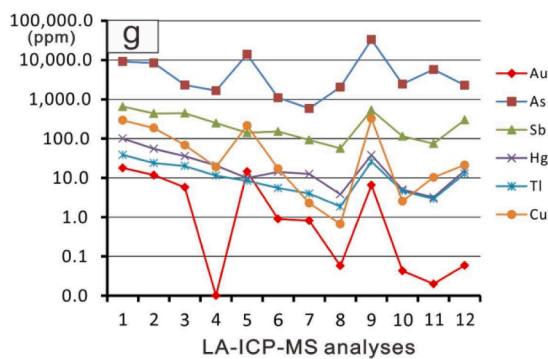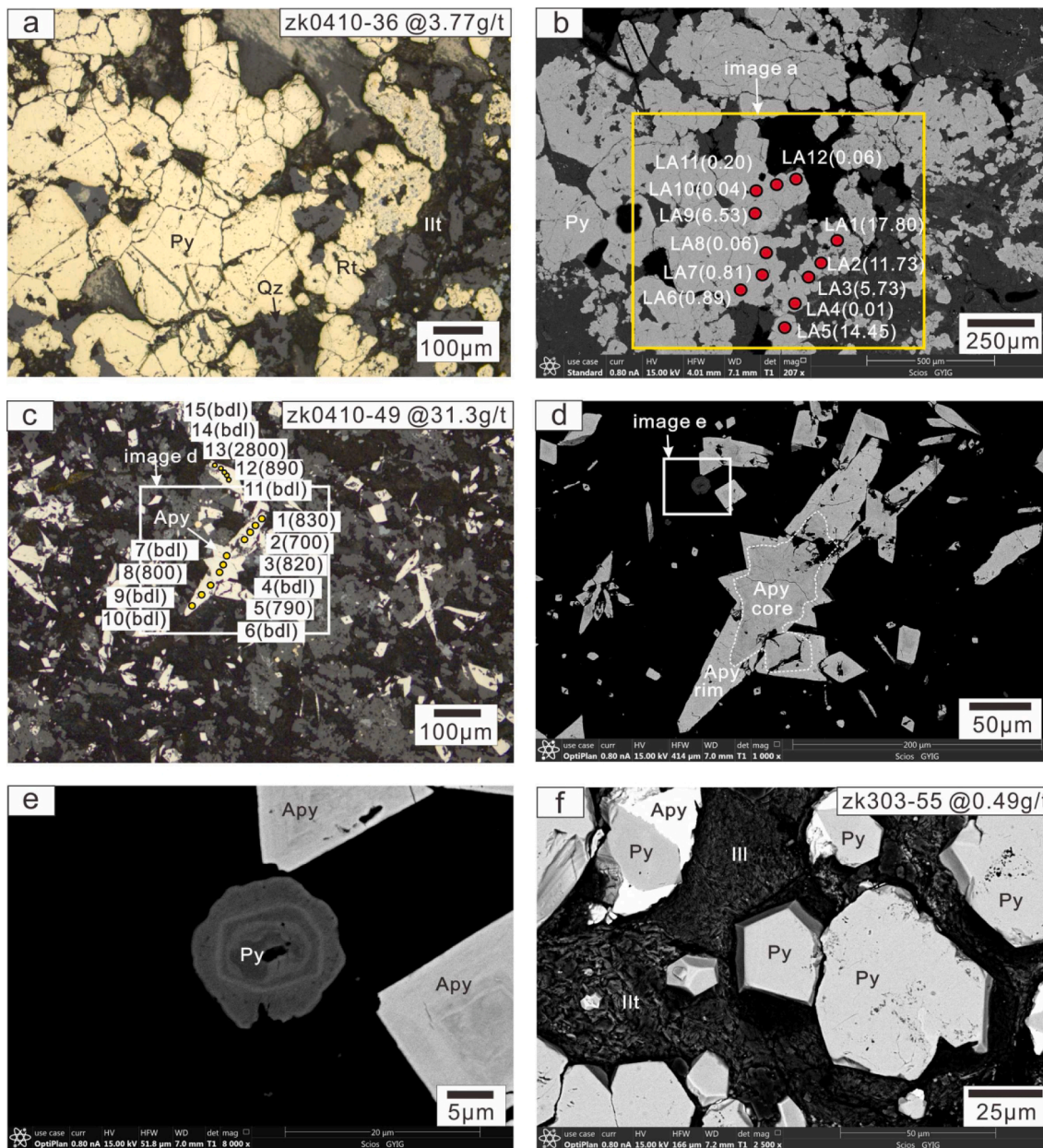
(caption on next page)

Fig. 13. Images of medium- and high-grade ore showing ore pyrite and arsenopyrite, and the distribution of trace elements in the ore pyrite and arsenopyrite, Jiadi (a-e, g-h) and Damaidi (f) deposits. The label in the top right of images a, c, and f indicates the sample number, consisting of drill hole number and sampling depth (meter), and Au grade. Red dots on image b and yellow dots on image c indicate locations of LA-ICP-MS and EPMA analyses, respectively, and were marked with analysis number and Au concentration in ppm. All LA-ICP-MS and EPMA data are listed in Tables 2 and 4, respectively. a-b. photomicrograph (a) and backscattered electron image (b) show the characteristic subhedral-anhedral ore pyrite. Zoning is commonly absent from the pyrite, although it is locally observed (e). Spider diagram of LA-ICP-MS data shows the distribution of Carlin-suite elements in ore pyrite, and the pyrite grain with high concentrations of As commonly has high concentrations of Au (g). c-e. photomicrograph (c) shows the subhedral-euhedral ore arsenopyrite has a homogeneous appearance; however, backscattered electron imaging adjusted for low brightness and high contrast shows the core is darker than the rim, and the boundary is irregular (d, e). Spider diagram of EPMA data show the dark core corresponding with the low concentration of As (h). f. Ore pyrite commonly has a homogeneous appearance, and locally is encompassed by ore arsenopyrite. Abbreviations: Apy = arsenopyrite, Ilt = illite, Py = pyrite, Qz = quartz, Rt = rutile.

experienced rifting, passive-margin sequence deposition of sedimentary rocks, orogenic deformation, and late extension (Su et al., 2018; Xie et al., 2018a; Wang et al., 2020). (2) The basalt-hosted Au deposits are controlled by a regional structure (SBT) and which also controls a number of sediment-hosted Carlin-type Au deposits in the basin (Liu et al., 2010). (3) For both basalt-hosted and sediment-hosted Au deposits, elements associated with Au mineralization include As, Sb, Hg, Tl, and Cu, with low base metals, a typical characteristic of Carlin-type Au mineralization (Hofstra and Cline, 2000; Cline et al., 2005; Muntean et al., 2011; Muntean, 2018). (4) Both basalt-hosted and sediment-hosted Au deposits formed from ore fluids with relatively low temperature and low salinity (Zhang et al., 2003; Su et al., 2009, 2018; Wang, 2015). (5) Some of the alteration minerals and processes for both basalt-hosted and sediment-hosted Au deposits are similar, including formation of disseminated arsenian pyrite, arsenopyrite, jasperoid quartz, illite, and (Fe)-dolomite. Additionally, the late-ore stage minerals for both are almost the same, including open-space filling realgar, calcite, quartz, stibnite, and orpiment. (6) Arsenian pyrite and arsenopyrite are the dominating Au-bearing minerals, although arsenopyrite in basalt-hosted Au deposits is more abundant than in sediment-hosted Au deposits. The Au-bearing sulfide minerals formed during sulfidation, a primary Au deposition mechanism in Carlin-type Au deposits (Hofstra et al., 1991; Stenger et al., 1998; Kesler et al., 2003; Ye et al., 2003; Xie et al., 2018a). Gold in the Au-bearing minerals is invisible using microscopy and SEM analyses, a key characteristic of Carlin-type Au mineralization (Hofstra and Cline, 2000; Cline et al., 2005). The invisible Au is proposed to be incorporated into the arsenian pyrite and arsenopyrite mainly as ionic Au (Au^{1+}) (Simon et al., 1999a, 1999b; Reich et al., 2005; Deditius et al., 2014; Gopon et al., 2019; Liang et al., 2020). (7) Sulfur isotope compositions of ore-related minerals for both basalt-hosted and sediment-hosted Au deposits are ~0‰ (Hu et al., 2018; Xie et al., 2018b), possibly reflecting a uniform origin for these deposits.

A key difference between the basalt-hosted and sediment-hosted Au deposits, excepting the host rocks, includes some of the alteration minerals and processes. In the basalt-hosted Au deposits, ore-stage rutile and apatite are commonly observed, however, they are rarely observed in sediment-hosted Au deposits (Hu et al., 2002; Su et al., 2018; Xie et al., 2018a). This is a result of the difference in host rocks. If the near-neutral ore fluid reacted with sedimentary rocks, the fluid would have sulfidized the Fe in Fe-dolomite to form ore-stage dolomite and Au-bearing arsenian pyrite and arsenopyrite (Xie et al., 2017, 2018a). In addition, fluid-rock reaction results in decarbonization and silicification of calcite and formation of jasperoid quartz, and argillization of K-bearing minerals (e.g. mica and K-feldspar) and formation of illite (Xie et al., 2017, 2018a; Su et al., 2018). However, where the ore fluid reacted with basalt, fluid sulfidized Fe primarily from the ilmenite and magnetite to produce rutile and Au-bearing arsenian pyrite and arsenopyrite (Fig. 14). Additionally, the ore fluid reacted with and altered orthopyroxene, clinopyroxene, and plagioclase to jasperoid quartz, (Fe)-dolomite (locally Ca-Mg-siderite), illite, and apatite (Fig. 14). Because Fe in the basalt (Fe_2O_3: ~14 wt%) generally exceeds the amount needed for sulfidation, significant Fe after sulfidation is available in the ore fluid and locally Ca-Mg-siderite formed.

Another difference from the sediment-hosted deposits is the

elemental flux associated with Au mineralization. In the sediment-hosted Au deposits, Au mineralization is associated with the addition of Si to form jasperoid quartz, plus K immobility or loss (Cail and Cline, 2001; Tan et al., 2015a). In contrast, in basalt-hosted Au deposits, Si remains nearly constant, whereas K is significantly added to the rock (Figs. 6; 7; 8). This suggests that the ore fluid is enriched in K and Si. In sediment-hosted Au deposits, the available K in calcareous sedimentary rocks is sufficient for formation of illite. However, because the available Si in calcareous sedimentary rocks is insufficient for formation of quartz and silicates, Si from the ore fluid was added to the ore assemblage. Similarly, in basalt-hosted Au deposits, because the basalt contained sufficient available Si, but insufficient K, significant K from the fluid was fixed in the ore assemblage.

A comparison of results shows that the Jiadi and Damaidi Au deposits share remarkable similarities to the Guizhou sediment-hosted Carlin-type Au deposits although they have some differences. The sediment-hosted and basalt-hosted deposits both likely formed in response to the same metallogenic event. All Guizhou Carlin-type Au deposits share consistently similar geologic characteristics, especially the ~-5-+5‰ S isotope composition of ore-related sulfide minerals (Xie et al., 2018b), reflecting that these deposits possibly formed in response to a widespread magmatic hydrothermal event (Xie et al., 2018b; Jin et al., 2020). However, the metamorphic hydrothermal origin (Su et al., 2009, 2018) and meteoric fluid origin (Hu and Zhou, 2012; Hu et al., 2017) can't be ruled out.

6. Conclusions and implications

This study establishes the mineral parageneses of the Jiadi and Damaidi deposits (Fig. 10). Gold mineralization accompanied the formation of disseminated arsenian pyrite, arsenopyrite, illite, jasperoid quartz, (Fe)-dolomite (locally Ca-Mg-siderite), and minor rutile and apatite. Ionic Au is invisible in arsenian pyrite and arsenopyrite which formed during sulfidation of Fe in the basalt. Late-ore stage minerals, including realgar, calcite, quartz, stibnite, and orpiment, precipitated in open space as the hydrothermal system cooled and collapsed. Locally, minor oxide minerals (e.g. hematite) and chlorite formed during post-ore oxidation.

The Jiadi and Damaidi basalt-hosted Au deposits exhibit remarkable similarity to Guizhou sediment-hosted Carlin-type deposits, and both can be classified as Carlin-type Au deposits. The major difference is that the basalt-hosted deposits contain abundant ore-stage Fe-dolomite (locally Ca-Mg-siderite) and rutile in ore, which are absent from the sediment-hosted Au deposits. This is because the Emeishan basalt contains high concentrations of available Fe and Ti, sufficient for the formation of Fe-dolomite (locally Ca-Mg-siderite) and rutile, respectively. The basalt-hosted and sediment-hosted Carlin-type Au deposits in Dian-Qian-Gui area formed in response to the same widespread metallogenic event.

This study suggests that basalt is a potential host rock for Carlin-type Au mineralization because it is enriched in Fe, providing available Fe for sulfidation and formation of Au-bearing pyrite and arsenopyrite. The Emeishan basalt is widely distributed in the northwestern margin of the Youjiang basin (Fig. 1), and unconformably overlies the Upper Permian

Table 2

Laser ablation-inductively coupled plasma-mass spectrometry analyses of pyrite in the Jiadi deposit (ppm).

Analysis No.	Mineral	Au	As	Sb	Hg	Tl	Cu	Na	Mg	Al	Si	S	K	Ca	Sc	Ti	V	Cr
Fig. 13b (zk0410-36, 3.77 g/t, Jiadi deposit)																		
1	Pyrite	17.80	9189	655.5	101	38.35	291.7	89	330	4423	7570	579,586	1576	1282	9.1	43,345	629.2	2
2	Pyrite	11.73	8412	434.4	55	23.81	185.8	73	247	3592	5693	551,235	1438	3254	31.2	74,455	374.7	17
3	Pyrite	5.73	2305	442.0	36	20.03	67.9	64	275	2122	3920	630,435	854	bdl	0.9	41	12.0	0
4	Pyrite	0.01	1659	248.1	21	11.42	18.9	27	65	1444	2183	609,354	498	214	0.0	bdl	6.9	1
5	Pyrite	14.45	13,929	140.5	10	8.37	214.5	22	236	265	5	567,479	151	646	0.6	722	16.2	bdl
6	Pyrite	0.89	1093	151.7	14	5.51	17.1	17	682	292	309	608,285	97	4100	4.0	1	2.8	1
7	Pyrite	0.81	587	92.0	13	3.96	2.3	2	15	342	576	608,283	146	12	0.0	bdl	1.6	1
8	Pyrite	0.06	2048	56.6	4	1.86	0.7	3	12	378	1460	603,913	123	382	0.3	0	1.2	3
9	Pyrite	6.53	33,062	534.1	38	26.06	322.4	69	115	3538	5211	524,892	1471	0	1.0	4	15.9	bdl
10	Pyrite	0.04	2436	114.7	5	4.58	2.5	6	16	396	1407	628,466	163	22	bdl	1	2.3	bdl
11	Pyrite	0.02	5758	74.6	3	2.91	10.3	10	17	475	1121	595,603	235	185	bdl	1	2.7	5
12	Pyrite	0.06	2283	298.2	15	12.76	21.3	43	82	1511	2312	637,121	582	112	0.5	5	7.0	bdl

Analysis No.	Mineral	Mn	Fe	Co	Ni	Zn	Ga	Ge	Se	Rb	Sr	Y	Mo	Ag	Cd	In	Sn	Te	Ba	W	Bi	Pb	Th	U
Fig. 13b (zk0410-36, 3.77g/t, Jiadi deposit)																								
1	Pyrite	32	348,921	799.1	401.7	7	5.9	15	6	12.5	79.11	23.35	0.5	17.2	5	0.01	9	0.4	153.7	318.3	0.22	57.36	2.13	0.79
2	Pyrite	27	349,829	19.4	10.3	13	4.7	12	bdl	8.0	64.06	25.75	0.4	9.5	10	0.10	14	1.7	107.6	275.1	0.34	34.63	1.96	0.86
3	Pyrite	38	359,098	151.1	58.3	9	1.6	11	5	3.5	1.69	0.10	bdl	4.5	2	0.18	1	bdl	3.5	0.7	0.04	11.76	0.01	bdl
4	Pyrite	1	384,193	22.0	4.3	2	1.4	13	1	2.4	0.17	0.01	0.1	0.0	2	0.08	1	0.4	2.7	0.0	bdl	1.58	bdl	bdl
5	Pyrite	54	415,948	68.5	14.6	3	0.2	11	1	0.5	3.27	0.42	0.2	5.0	2	0.02	0	bdl	1.7	15.2	0.08	10.09	0.03	bdl
6	Pyrite	154	384,734	12.0	0.8	3	0.1	8	1	0.4	7.03	0.19	0.1	0.2	2	0.11	1	bdl	0.8	bdl	0.03	2.56	bdl	bdl
7	Pyrite	3	389,875	19.1	3.0	2	0.2	12	bdl	0.8	0.32	bdl	0.3	0.1	2	0.03	2	0.2	0.6	0.0	bdl	1.70	bdl	bdl
8	Pyrite	4	391,575	2.9	0.2	2	0.2	11	1	0.4	0.02	bdl	0.1	bdl	bdl	0.01	1	0.2	0.6	0.0	bdl	0.38	bdl	bdl
9	Pyrite	2	430,631	7.2	4.1	6	3.0	12	bdl	6.1	0.91	0.58	bdl	2.4	1	0.02	1	bdl	7.0	bdl	0.02	9.35	0.03	bdl
10	Pyrite	1	366,937	1.4	0.2	2	0.6	10	1	1.9	0.13	bdl	bdl	0.1	bdl	0.02	bdl	bdl	1.0	0.0	bdl	0.94	bdl	bdl
11	Pyrite	1	396,452	19.4	6.9	1	0.6	9	3	0.7	0.10	0.20	bdl	bdl	1	0.03	bdl	0.2	1.9	0.0	bdl	1.26	0.05	0.01
12	Pyrite	3	355,448	74.3	33.3	7	0.9	12	bdl	3.5	1.26	0.01	0.1	0.2	bdl	0.03	bdl	bdl	4.0	0.1	0.02	5.27	0.04	bdl

bdl = below detection limit.

Table 3

Average values of elements in pyrite and arsenopyrite from EPMA in the Jiadi and Damaidi deposits (in ppm).

Pyrite/arsenopyrite	Deposit	Fe	Cu	Zn	Co	Ni	Bi	Au	As	S	Sb	Hg	Tl	Te	Pb
Pyrite	Jiadi	444,884	167	97	380	45	691	445	21,194	528,823	95	bdl	3	19	53
Pyrite	Damaidi	443,868	142	128	381	95	655	478	6633	544,458	48	bdl	bdl	26	76
Pyrite	Jiadi and Damaidi	444,520	158	108	380	63	678	457	15,974	534,428	78	bdl	2	22	61
Arsenopyrite	Jiadi	346,442	167	50	428	102	380	503	399,615	240,147	327	bdl	114	13	317
Arsenopyrite	Damaidi	346,328	263	60	290	38	293	616	408,399	234,242	113	bdl	46	13	317
Arsenopyrite	Jiadi and Damaidi	346,389	212	55	363	72	339	556	403,738	237,375	227	bdl	82	13	317

Data used to calculate the average value are listed in Table A4; We use 0 if the analysis is below detection limit. bdl = below detection limit.
Pyrite: N = 159 (102 analyses from Jiadi and 57 analyses from Damaidi); Arsenopyrite: N = 49 (26 analyses from Jiadi and 23 analyses from Damaidi)

Table 4

Electron probe microanalysis of arsenopyrite in the Jiadi deposit (ppm).

| Analysis No.	Mineral	Fe	Cu	Zn	Co	Ni	Bi	Au	As	S	Sb	Hg	Tl	Te	Pb	Total
Fig. 13c (zk0410-49, 31.3 g/t, Jiadi deposit)																
1	Arsenopyrite	334,020	bdl	60	420	210	940	830	454,130	206,780	50	bdl	810	bdl	470	99.9
2	Arsenopyrite	342,490	bdl	90	230	100	290	700	423,530	227,040	70	bdl	bdl	bdl	bdl	99.5
3	Arsenopyrite	342,970	bdl	bdl	400	bdl	1900	820	425,820	226,330	1030	bdl	220	bdl	430	100.0
4	Arsenopyrite	357,830	490	290	580	bdl	890	bdl	343,560	279,500	370	bdl	280	bdl	bdl	98.4
5	Arsenopyrite	356,520	350	80	330	210	bdl	790	369,350	268,320	130	bdl	bdl	bdl	bdl	99.6
6	Arsenopyrite	344,900	530	bdl	210	bdl	620	bdl	405,600	234,650	190	bdl	bdl	bdl	bdl	98.7
7	Arsenopyrite	360,410	140	bdl	240	bdl	770	bdl	366,880	261,320	70	bdl	bdl	bdl	590	99.0
8	Arsenopyrite	353,300	240	30	520	bdl	bdl	800	371,790	255,620	470	bdl	460	bdl	bdl	98.3
9	Arsenopyrite	341,290	bdl	bdl	170	340	70	bdl	419,210	225,160	770	bdl	1050	bdl	bdl	98.8
10	Arsenopyrite	333,570	60	bdl	90	bdl	220	bdl	418,950	220,710	230	bdl	bdl	bdl	bdl	97.4
11	Arsenopyrite	356,580	100	bdl	800	bdl	260	bdl	370,200	260,810	270	bdl	bdl	bdl	170	98.9
12	Arsenopyrite	368,060	140	bdl	210	bdl	410	890	335,460	286,130	80	bdl	bdl	bdl	390	99.2
13	Arsenopyrite	341,230	bdl	40	480	bdl	400	2800	415,020	223,910	190	bdl	110	bdl	bdl	98.4
14	Arsenopyrite	340,040	470	160	70	40	bdl	bdl	425,880	225,150	890	bdl	bdl	bdl	720	99.3
15	Arsenopyrite	341,240	200	200	430	bdl	bdl	bdl	428,860	222,530	190	bdl	bdl	bdl	bdl	99.4

bdl = below detection limit.
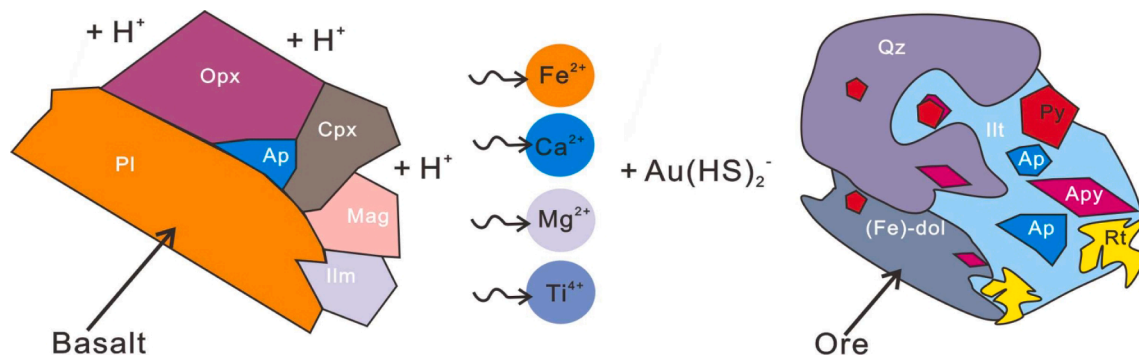
Fig. 14. Schematic diagram showing the process of ore fluid reacting with basalt. The near-neutral ore fluid reacts with the basalt consisting of plagioclase (Pl, Na[AlSi$_3$O$_8$]-Ca[Al$_2$Si$_2$O$_8$]), orthopyroxene (Opx, (Mg, Fe)$_2$[(Si, Al)$_2$O$_6$]), clinopyroxene (Cpx, (Ca, Mg, Fe, Al, Ti)$_2$[(Si, Al)$_2$O$_6$]), magnetite (Mag, Fe$_3$O$_4$), ilmenite (Ilm, FeTiO$_3$) and apatite (Ap, Ca$_5$(PO$_4$)$_3$(F, Cl, OH)), which results in releasing of Fe^{2+}, Ca^{2+}, Mg^{2+}, Ti^{4+}, and et cetera from the basalt. The released ions react with the Au(HS)$_2^-$ -rich ore fluid, and Au-bearing pyrite (Py) and arsenopyrite (Apy), quartz (Qz), illite (Ilt), (Fe)-dolomite ((Fe)-dol), rutile (Rt), and apatite (Ap) form.

Moukou Formation (Figs. 3, 4). The regional SBT acted as ore fluid channel, and fed ore fluids that reacted with active and permeable basalt. Anticlines above the unconformity facilitated ore fluid porosity, permeability, and fluid-rock reaction that led to ore formation. Thus, future Carlin-type Au exploration in Dian-Qian-Gui area should continue to focus on area covered by basalt, especially where anticlines above the unconformity occur between the Maokou Formation and Emeishan basalt. Additionally, the presence of jasperoid quartz, (Fe)-dolomite, and illite indicate large-scale fluid-rock reaction, and may indicate the nearby presence of Au mineralization. Late-ore stage realgar, calcite,
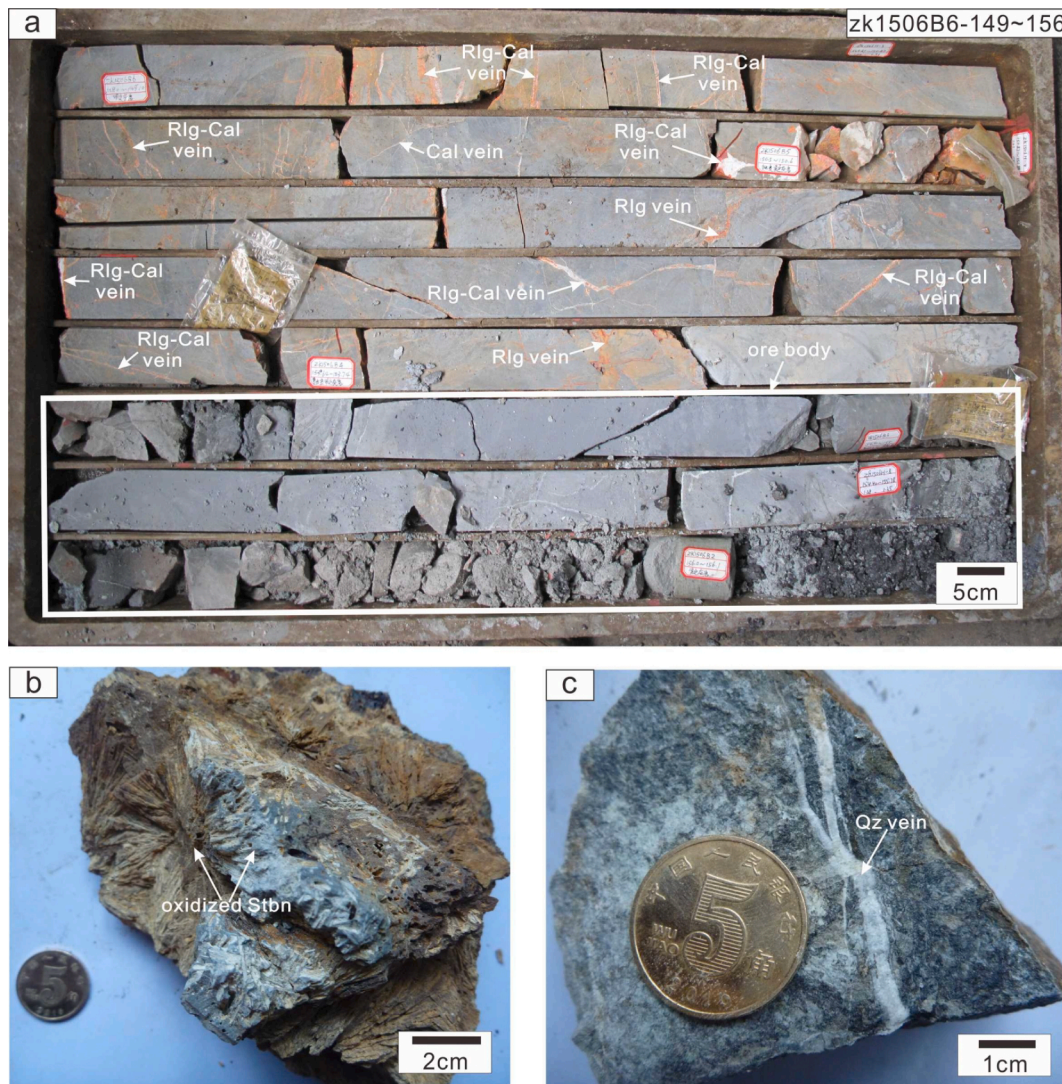
Fig. 15. Images showing late-ore stage minerals from the Jiadi (a) and Damaidi (b, c) deposits. A. Abundant realgar and calcite veins occur near the orebody. b, The radial stibnite precipitates in open space, and is locally oxidized. c. A quartz vein crosscuts ore. Abbreviations: Cal = calcite, Qz = quartz, Rlg = realgar, Stbn = stibnite.

Table 5
Comparison of the Jiadi and Damaidi deposits with Guizhou sediment-hosted Carlin-type Au deposits.

	Guizhou sediment-hosted Carlin-type Au deposits	Jiadi and Damaid basalt-hosted Au deposits
Tectonic setting	The region experienced rifting, passive-margin sequence deposition, orogenic deformation, and late extension	The same with sediment-hosted Carlin-type Au deposits
Host rock	Mainly bioclastic limestone and calcareous siltstone and sandstone	Basaltic conglomerate and basaltic tuff
Ore-controlling structure	Anticline, unconformity, and fault	Secondary crumpled tectonic zone of the Lianhuashan anticline, unconformity, and fault
Mineralization style	Strata-bound and fault-controlled mineralization	Mainly strata-bound mineralization and locally fault-controlled mineralization
Geochemical signature	Au, As, Sb, Hg, Tl, and Cu	Au, As, Sb, Hg, Tl, and Cu
Ore fluid temperature and chemistry	Low-intermediate temperature (190–300 °C), low salinity ($<\sim$5 wt% NaCl equiv.), CO_2-rich (6–75 mol %), reduced, and non-boiling ore fluids	Low-intermediate temperature (190–230 °C) and low salinity (4–8 wt% NaCl equiv.) ore fluids.
Ore mineral	Including disseminated arsenian pyrite and minor arsenopyrite; Ore minerals enriched in Au, As, Sb, Hg, Tl, and Cu; Gold is invisible in the ore minerals	Including disseminated arsenian pyrite and minor arsenopyrite; Ore minerals enriched in Au, As, Sb, Hg, Tl, and Cu; Gold is invisible in the ore minerals
Alteration minerals and process	Decarbonization of calcite, silicificaiton of calcite and formation of jasperoid quartz, argillization of K-bearing minerals and formation of illite, and sulfidation of Fe from Fe-dolomite and formation of dolomite, arsenian pyrite and minor arsenopyrite	Ore fluid reacts with orthopyroxene, clinopyroxene, and plagioclase from basalt, resulting in formation of jasperoid quartz, (Fe)-dolomite, illite, and apatite. Sulfidation of Fe from ilmenite and magnetite and precipitation of rutile, arsenian pyrite and arsenopyrite
Late-ore stage mineral	Realgar, calcite, quartz, stibnite, and orpiment	Realgar, calcite, quartz, stibnite, and orpiment
Sulfur isotope composition of ore-related minerals	Ranging from $\sim$-5 to $\sim$ 5‰, mainly around 0‰; Locally >10‰	Ranging from $\sim$-3 to $\sim$2‰, mainly around 0‰
Ore deposition mechanism	Sulfidation of Fe from host rocks and deposition of Au-bearing pyrite and minor arsenopyrite.	Sulfidation of Fe from host rocks and deposition of Au-bearing pyrite and arsenopyrite.
Main references	Hu et al., 2002, 2017; Su et al., 2009, 2018; Xie et al., 2018a, 2018b	Wang, 2015; Hu et al., 2018; This study

stibnite, vein quartz, and orpiment commonly precipitated in open space near and around the orebody, thus may suggest the nearby presence of Au mineralization.

Declaration of Competing Interest

The authors declare that they have no known competing financial interests or personal relationships that could have appeared to influence the work reported in this paper.

Acknowledgements

Appendix A. Supplementary data

Supplementary data to this article can be found online at https://doi.org/10.1016/j.oregeorev.2021.104034.

References

Cail, T.L., Cline, J.S., 2001. Alteration associated with gold deposition at the Getchell Carlin-type gold deposit, north-central Nevada. Econ. Geol. 96 (6), 1343–1359.

Chen, M.H., Mao, J.W., Chen, Z.Y., Zhang, W., 2009. Mineralogy of arsenian pyrites and arsenopyrites of Carlin-type gold deposits in Yunnan-Guizhou-Guangxi "golden triangle" area, southwestern China. Mineral Deposits 28, 539–557 (in Chinese with English abstract).

Chen, M.H., Mao, J.W., Bierlein, F.P., Norman, T., Uttley, P.J., 2011. Structural features and metallogenesis of the Carlin-type Jinfeng (Lannigou) gold deposit, Guizhou Province. China. Ore Geol. Rev. 43 (1), 217–234.

Chen, M.H., Zhang, Y., Meng, Y.Y., Lu, G., Liu, S.Q., 2014. The confirmation of the upper limit of metallogenetic epoch of Liaotun gold deposit in western Guangxi, China, and its implication on chronology of Carlin-type gold deposits in Yunnan-Guizhou-Guangxi "Golden Triangle" area. Mineral Depos. 33, 1–13 (in Chinese with English abstract).

Cline, J.S., 2001. Timing of gold and arsenic sulfide mineral deposition at the Getchell Carlin-type gold deposit, north-central Nevada. Econ. Geol. 96 (1), 75–89.

Cline, J.S., Hofstra, A.H., Muntean, J.L., Tosdal, R.M., Hickey, K.A., 2005. Carlin-type gold deposits in Nevada: Critical geologic characteristics and viable models, in: Hedenquist, J.W., Thompson, J.F.H., Goldfarb, R.J., Richards, J.P. (Eds.), Econ. Geol. 100th Anniversary Volume. Society of Economic Geologists, Inc., Littleton, pp. 451-484.

Cline, J.S., Muntean, J.L., Gu, X.X., Xia, Y., 2013. A comparison of Carlin-type deposits: Guizhou Province, golden triangle, southwest China, and northern Nevada, USA. Earth Sci. Front. 20 (1), 1–18.

Deditius, A.P., Reich, M., Kesler, S.E., Utsunomiya, S., Chryssoulis, S.L., Walshe, J., Ewing, R.C., 2014. The coupled geochemistry of Au and As in pyrite from hydrothermal ore deposits. Geochim. Cosmochim. Ac. 140, 644–670.

Finlow-Bates, T., Stumpfl, E.F., 1981. The behaviour of so-called immobile elements in hydrothermally altered rocks associated with volcanogenic submarine-exhalative ore deposits. Miner. Deposita 16 (2), 319–328.

Frimmel, H.E., 2008. Earth's continental crustal gold endowment. Earth. Planet. Sci. Lett. 267 (1–2), 45–55.

Gopon, P., Douglas, J.O., Auger, M.A., Hansen, L., Wade, J., Cline, J.S., Robb, L.J., Moody, M.P., 2019. A nanoscale investigation of Carlin-type gold deposits: An atom-scale elemental and isotopic perspective. Econ. Geol. 98 (6), 1123–1133.

Grant, J.A., 1986. The isocon diagram-a simple solution to Gresens' equation for metasomatic alteration. Econ. Geol. 81 (8), 1976–1982.

Gresens, R.L., 1967. Composition-volume relationships of metasomatism. Chem. Geol. 2, 47–65.

Guo, F., Fan, W.M., Wang, Y.J., Li, C.W., 2004. When did the Emeishan mantle plume activity start? Geochronological and geochemical evidence from ultramafic-mafic dikes in Southwestern China. Int. Geol. Rev. 46 (3), 226–234.

Guo, S., Ye, K., Chen, Y., Liu, J.B., Mao, Q., Ma, Y.G., 2012. Fluid-rock interaction and element mobilization in UHP metabasalt: Constraints from an omphacite-epidote vein and host eclogites in the Dabie orogen. Lithos 136–139, 145–167.

Hofstra, A.H., 1994. Geology and genesis of the Carlin-type gold deposits in the Jerritt Canyon district, Nevada. Ph.D. dissertation, Boulder, Colorado, University of Colorado, p. 719.

Hofstra, A.H., Cline, J.S., 2000. Characteristics and models for Carlin- type gold deposits, in: Hagemann, S.G., Brown, P.E. (Eds.), Gold in 2000. Rev. Econ. Geol. 13, Society of Economic Geologists Inc., Littleton, pp.163-220.

Hofstra, A.H., Leventhal, J.S., Northrop, H.R., Landis, G.P., Rye, R.O., Birak, D.J., Dahl, A.R., 1991. Genesis of sediment-hosted disseminated-gold deposits by fluid mixing and sulfidization: Chemical-reaction-path modeling of ore-depositional processes documented in the Jerritt Canyon district. Nevada. Geology 19 (1), 36–40.

Hu, R.Z., Fu, S.L., Huang, Y., Zhou, M.F., Fu, S.H., Zhao, C.H., Wang, Y.J., Bi, X.W., Xiao, J.F., 2017. The giant South China Mesozoic low-temperature metallogenic domain: Reviews and a new geodynamic model. J. Asian. Earth. Sci. 137, 9–34.

Hu, R.Z., Su, W.C., Bi, X.W., Tu, G.Z., Hofstra, A., 2002. Geology and geochemistry of Carlin-type gold deposits in China. Miner. Deposita 37, 378–392.

Hu, R.Z., Zhou, M.F., 2012. Multiple Mesozoic mineralization events in South China-an introduction to the thematic issue. Miner. Deposita 47, 579–588.

Hu, X.L., Zeng, G.P., Zhang, Z.J., Li, W.T., Liu, W.H., Gong, Y.J., Yao, S.Z., 2018. Gold mineralization associated with Emeishan basaltic rocks: Mineralogical, geochemical, and isotopic evidences from the Lianhuashan ore field, southwestern Guizhou Province. China. Ore Geol. Rev. 95, 604–619.

Lai, C.K., Meffre, S., Crawford, A.J., Zaw, K., Xue, C.D., Halpin, J.A., 2014. The western Ailaoshan volcanic belts and their SE Asia connection: A new tectonic model for the eastern Indochina block. Gondwana Res. 43 (1), 217–234.

Li, Z.X., L. X.H, 2007. Formation of the 1300-km-wide intracontinental orogen and postorogenic magmatic province in Mesozoic South China: A flat-slab subduction model. Geology 35 (2), 179–182.

Jin, X.Y., Hofstra, A.H., Hunt, A.G., Liu, J.Z., Yang, W., Li, J.W., 2020. Noble gases fingerprint the source and evolution of ore-forming fluids of Carlin-type gold deposits in the golden triangles. South China. Econ. Geol. 115 (2), 455–469.

Kesler, S.E., Fortuna, J., Ye, Z.J., Alt, J.C., Core, D.P., Zohar, P., Borhauer, J., Chryssoulis, S.L., 2003. Evaluation of the role of sulfidation in deposition of gold, Screamer section of the Betze-Post Carlin-type deposit. Nevada. Econ. Geol. 98 (6), 1137–1157.

Liang, Q.L., Xie, Z.J., Song, X.Y., Wirth, R., Xia, Y., Cline, J., 2020. Evolution of invisible Au in arsenian pyrite in Carlin-type Au deposits. Econ, Geol in press.

Liu, J.Z., Yang, C.F., Xia, Y., Chen, S., Chen, F.E., Fu, Z.K., 2010. SBT study and ideas in platform facies area in the southwest Guizhou. Guizhou Geology 27 (4), 178–184 (in Chinese with English abstract).

Liu, J.Z., Xia, Y., Tao, Y., Yang, C.F., Wang, Z.P., Tan, Q.P., Fu, S.H., Chen, R., Wu, W.M., 2014. The relation between SBT and gold-antimony deposit metallogenesis and prospecting in southwest Guizhou. Guizhou Geology 31 (4), 267–272 (in Chinese with English abstract).

Liu, Y.H., 2002. Analysis on the minerogenetic geological condition of the gold ore in the Lianhuashan anticline, western Guizhou. Guizhou Geology 19 (4), 231–234 (in Chinese with English abstract).

Maroun, L.R.C., Cline, J.S., Simon, A., Anderson, P., Muntean, J.L., 2017. High-grade gold deposition and collapse breccia formation, Cortez Hills Carlin-type gold deposit, Nevada. USA. Econ. Geol. 112 (4), 707–740.

Muntean, J.L., 2018. The Carlin gold system: Applications to exploration in Nevada and beyond, in: Muntean, J.L. (Ed.), Diversity in Carlin-style gold deposits. Rev. Econ. Geol. 20, Society of Economic Geologists Inc., Littleton, pp. 39-88.

Muntean, J.L., Cline, J.S., 2018. Diversity of Carlin-style gold deposits, in: Muntean, J.L. (Ed.), Diversity in Carlin-style gold deposits. Rev. Econ. Geol. 20, Society of Economic Geologists Inc., Littleton, pp. 1-6.

Muntean, J.L., Cline, J.S., Simon, A.C., Longo, A.A., 2011. Magmatic-hydrothermal origin of Nevada's Carlin-type gold deposits. Nat. Geosci. 4 (2), 122–127.

Reich, M., Kesler, S.E., Utsunomiya, S., Palenik, C.S., Chryssoulis, S.L., Ewing, R.C., 2005. Solubility of gold in arsenian pyrite. Geochim. Cosmochim. Ac. 69 (11), 2781–2796.

Simon, G., Huang, H., Penner-Hahn, J.E., Kesler, S.E., Kao, L.S., 1999a. Oxidation state of gold and arsenic in gold-bearing arsenian pyrite. Am. Mineral. 84, 1071–1079.

Simon, G., Kesler, S.E., Chryssoulis, S., 1999b. Geochemistry and textures of gold-bearing arsenian pyrite, Twin Creeks, Nevada: Implications for deposition of gold in Carlin-type deposits. Econ. Geol. 94 (3), 405–421.

Stenger, D.P., Kesler, S.E., Peltonen, D.R., Tapper, C.J., 1998. Deposition of gold in Carlin-type deposits: The role of sulfidation and decarbonation at Twin Creeks. Nevada. Econ. Geol. 93 (2), 201–215.

Su, W.C., Dong, W.D., Zhang, X.C., Shen, N.P., Hu, R.Z., Hofstra, A. H., Cheng, L.Z., Xia, Y., Yang, K.Y., 2018. Carlin-type gold deposits in the Dian-Qian-Gui "golden triangle" of southwest China, in: Muntean, J.L. (Ed.), Diversity in Carlin-style gold deposits. Rev. Econ. Geol. 20, Society of Economic Geologists Inc., Littleton, pp. 157-185.

Su, W.C., Heinrich, C.A., Pettke, T., Zhang, X.C., Hu, R.Z., Xia, B., 2009. Sediment-hosted gold deposits in Guizhou, China: Products of wall-rock sulfidation by deep crustal fluids. Econ. Geol. 104 (1), 73–93.

Su, W.C., Zhang, H.T., Hu, R.Z., Ge, X., Xia, B., Chen, Y.Y., Zhu, C., 2012. Mineralogy and geochemistry of gold-bearing arsenian pyrite from the Shuiyindong Carlin-type gold deposit, Guizhou, China: Implications for gold depositional processes. Miner. Deposita 47 (6), 653–662.

Tan, Q.P., Xia, Y., Xie, Z.J., Yan, J., 2015a. Migration paths and precipitation mechanisms of ore-forming fluids at the Shuiyindong Carlin-type gold deposit, Guizhou. China. Ore Geol. Rev. 69, 140–156.

Tan, Q.P., Xia, Y., Xie, Z.J., Yan, J., Wei, D.T., 2015b. S, C, O, H, and Pb isotopic studies for the Shuiyindong Carlin-type gold deposit, southwest Guizhou, China: Constraints for ore genesis. Chin. J. Geochem. 34 (4), 525–539.

Wang, D.F., 2015. A preliminary study on the geological and geochemical characteristics of the Jiadi gold deposit in Panxian, Guizhou. M. thesis, Guiyang, China, Guizhou University, p. 66 (in Chinese with English abstract).

Wang, Q.F., Groves, D., 2018. Carlin-style gold deposits, Youjiang Basin, China: tectono-thermal and structural analogues of the Carlin-type gold deposits, Nevada, USA. Miner. Deposita 53 (7), 909–918.

Wang, Q.F., Yang, L., Xu, X.J., Santosh, M., Wang, Y.N., Wang, T.Y., Chen, F.G., Wang, R. X., Gao, L., Liu, X.F., Yang, S.J., Zeng, Y.S., Chen, J.H., Zhang, Q.Z., Deng, J., 2020. Multi-stage tectonics and metallogeny associated with Phanerozoic evolution of the south China Block: A holistic perspective from the Youjiang Basin. Earth-sci. Rev. 211, 103405.

Wei, D.T., Xia, Y., Gregory, D.D., Steadman, J.A., Tan, Q.P., Xie, Z.J., Liu, X.J., 2020. Multistage pyrites in the Nibao disseminated gold deposit, southwestern Guizhou Province, China: Insights into the origin of Au from textures, in situ trace elements, and sulfur isotope analyses. Ore Geol. Rev. 122, 103446.

Xie, Z.J., Xia, Y., Cline, J.S., Koenig, A., Wei, D.T., Tan, Q.P., Wang, Z.P., 2018a. Are there Carlin-type Au deposits in China? A comparison between the Guizhou China and Nevada USA deposits, in: Muntean, J.L. (Ed.), Diversity in Carlin-style gold deposits. Rev. Econ. Geol. 20, Society of Economic Geologists Inc., Littleton, pp. 187-233.

Xie, Z.J., Xia, Y., Cline, J.S., Pribil, M.J., Koenig, A., Tan, Q.P., Wei, D.T., Wang, Z.P., Yan, J., 2018. Magmatic origin for sediment-hosted Au deposits, Guizhou Province, China: In situ chemistry and sulfur isotope composition of pyrites. Shuiyindong and Jinfeng deposits. Econ. Geol. 113 (7), 1627–1652.

Xie, Z.J., Xia, Y., Cline, J.S., Yan, B.W., Wang, Z.P., Tan, Q.P., Wei, D.T., 2017. Comparison of the native antimony-bearing Paiting gold deposit, Guizhou Province, China, with Carlin-type gold deposits, Nevada, USA. Miner. Deposita 52, 69–84.

Yan, J., Hu, R.Z., Liu, S., Lin, Y.T., Zhang, J.C., Fu, S.L., 2018. NanoSIMS element mapping and sulfur isotope analysis of Au-bearing pyrite from Lannigou Carlin-type Au deposit in SW China: New insights into the origin and evolution of Au-bearing fluids. Ore Geol. Rev. 92, 29–41.

Yang, L., Deng, J., Groves, D.I., Wang, Q.F., Zhang, L., Wu, W., Qin, K., Zhang, Q.Z., 2020. Recognition of two contrasting structural- and mineralogical-gold mineral systems in the Youjiang Basin, China-Vietnam: Orogenic gold in the south and Carlin-type in the north. Geosci. Front., in press.

Ye, Z.J., Kesler, S.E., Essene, E.J., Zohar, P.B., Borhauer, J.L., 2003. Relation of Carlin-type gold mineralization to lithology, structure and alteration: Screamer zone, Betze-Post deposit. Nevada. Miner. Deposita 38 (1), 22–38.

Zaw, K., Meffre, S., Lai, C.K., Burrett, C., Santosh, M., Graham, I., Manaka, T., Salam, A., Kamvong, T., Cromie, P., 2014. Tectonics and metallogeny of mainland Southeast Asia – A review and contribution. Gondwana Res. 26 (1), 5–30.

Zeng, G.P., Luo, D.W., Gong, Y.J., Hu, X.L., Li, H., 2018. Structures and implications for fluid migration in the Jiadi Carlin-type gold deposit, Guizhou Province, southwest China. Resour. Geol. 68, 373–394.

Zhang, X.C., Spiro, B., Halls, C., Stanley, C.J., Yang, K.Y., 2003. Sediment-hosted disseminated gold deposits in southwest Guizhou, PRC: Their geological setting and origin in relation to mineralogical, fluid inclusion, and stable-isotope characteristics. Int. Geol. Rev. 45 (5), 407–470.

Zhong, H., Zhu, W.G., 2006. Geochronology of layered mafic intrusions from the Pan-Xi area in the Emeishan large igneous province. SW China. Miner. Deposita 41 (6), 599–606.

Zhou, M.F., Malpas, J., Song, X.Y., Robinson, P.T., Keays, R.R., 2002. A temporal link between the Emeishan large igneous province (SW China) and the end-Guadalupian mass extinction. Earth. Planet. Sc. Lett. 196 (3–4), 113–122.

Zhou, M.F., Zhao, J.H., Qi, L., Su, W.C., Hu, R.Z., 2006. Zircon U-Pb geochronology and elemental and Sr-Nd isotope geochemistry of Permian mafic rocks in the Funing area. SW China. Contrib. Mineral. Petr. 151 (1), 1–19.